International Journal of Plasticity 147 (2021) 103106

Contents lists available at ScienceDirect

International Journal of Plasticity

journal homepage: www.elsevier.com/locate/ijplas

Short- to long-term deformation behavior, failure, and service life of amorphous polymers under cyclic torsional and multiaxial loadings

T. Barriere [a], A. Cherouat [b], X. Gabrion [a], S. Holopainen [*,c]

[a] Univ. Bourgogne Franche-Comté, FEMTO-ST Institute, CNRS/UFC/ENSMM/UTBM, Department of Applied Mechanics, Besançon-FR 25000, France

[b] Univ. Technology of Troyes, Laboratory of Automatic Generation of Meshing and Advanced Methods (GAMMA3), Troyes, France

[c] Tampere University, Department of Civil Engineering, Tampere FI-33014, Finland

ARTICLE INFO

Keywords:
Service life
Polymers
Failure
Ratcheting
Modeling
Experimentation

ABSTRACT

When investigating materials to be utilized, attention inevitably focuses on their resistance over the service life. Despite the popularity of amorphous polymers, ranging from their applications in structural components to their ability to increase the toughness of biocomposites, the investigation of their short- to long-term resistance has been considerably limited to date. Here, an improved testing equipment and model are proposed to describe the resistance of amorphous polymers under cyclic loadings. Two failure mechanisms are considered for the low- to high-cycle regimes: plastically induced and fatigue, and a history dependent fatigue damage model and a plastic evolution law with a relaxed shear resistance are proposed. Against state-of-the-art models, the proposed model is able to simulate the experimentally observed ultralow- to high-cycle failure and service life under torsional and multiaxial loads. The experimental and model results are similar, suggesting that the model is a capable tool for simulating costly and time-consuming tests. Interestingly, the predicted progress of material failure with plastic deformation was found to resemble the observed development of accumulated void volume. The failure (void volume) development strongly influenced the onset and growth of tertiary cyclic creep and thus, the entire service life. The amorphous structure also appeared to effectively resist failure under torsion.

1. Introduction

Amorphous glassy polymers (where glassy refers to the solid-state below the glass transition temperature T_g), as we know them today, have been used since the 1950s. The most commonly used amorphous polymers are polystyrene (PS), poly(methyl methacrylate) (PMMA), and polycarbonate (PC) (Buschow, 2001). Their widespread consideration in research and development is due to their favorable properties (e.g., cheap price, impact toughness, and optical clearness); therefore amorphous polymers currently represent highly important technological materials in structural components (windows, sporting goods, vehicles, etc.), aeronautic equipment (e.g., the cockpit canopy of the Lockheed Martin F-22 Raptor fighter), packaging, electronic ionic conductors, and printed surface coatings (using additive manufacturing) (Adams et al., 1998; Kang and Kan, 2017; Lei and Wu, 2019; Wang et al., 2016). Their

* Corresponding author.
E-mail address: sami.holopainen@tuni.fi (S. Holopainen).

https://doi.org/10.1016/j.ijplas.2021.103106
Received 8 April 2021; Received in revised form 2 August 2021;
Available online 11 September 2021

characteristics can be further improved with additives such as coupling agents and impact modifiers (Buschow, 2001; Kang and Kan, 2017). Hence, amorphous polymers are also used as ingredients to improve the toughness of biopolymers and bulk metallic glasses (BMGs) (Adams et al., 1998; Park et al., 2019; Sun et al., 2016) and to heal damaged materials (Patrick et al., 2016). However, all these applications may suffer from failure under cyclic loading processes. Because the concurrent failures of engineering components under cyclic fatigue loads can result in horrific accidents (e.g., the air disaster of China Airlines Flight 611) and tremendous financial losses, it is worth investigating and testing the fatigue resistance of materials. However, such tests are costly and time-consuming, and thus, it is also worth developing capable models to simulate resource-intensive tests and even to develop more resistant materials and their manufacturing (Frankberg et al., 2019).

Although amorphous polymers have a vast number of applications, to date, little work has been conducted on their modeling and simulation under multiaxial and long-term cyclic loadings (Bennett and Horike, 2018; Lu et al., 2016). The Boyce-Parks-Argon (BPA) constitutive model is suitable for predicting the large deformation of amorphous polymers and may be the most distinguished model in the field (Boyce et al., 1988). The microstructure is described by the eight-chain model as illustrated in Fig. 4(a). However, this model is elastic-viscoplastic and thus is limited by its inaccurate predictions of the peak yield strain, unloading response, creep, and recovery observed in corresponding tests (Barriere et al., 2019; Dreistadt et al., 2009; Holopainen and Wallin, 2012). Considering the cyclic deformation behavior, the most advanced and recent models are suitable solely for (semi-)crystalline polymers exhibiting elastic-viscoplastic (Qi et al., 2019), hyperelastic-viscoplastic (Garcia-Gonzalez et al., 2017; Shojaei and Volgers, 2018), or viscoelastic-viscoplastic behavior (Colac and Dusunceli, 2006; Haouala and Doghri, 2015), to mention only a few. Considering amorphous polymers, both viscoelastic and viscoplastic elements are required to accurately predict the yield stress and strain, softening, static creep/recovery (Holopainen, 2013), shape/area of the load loops, cyclic creep (ratcheting), and thus the cyclic deformation behavior (Barriere et al., 2020; Chen et al., 2015). Nevertheless, only a few models include both these elements, despite being demonstrated under solely 1D loads (Anand and Ames, 2006; Barriere et al., 2019; Janssen et al., 2008; Jiang et al., 2015; Krairi et al., 2019). Notable work has been performed to describe the development of fatigue failure by mechanical tests (Lu et al., 2016) and molecular dynamics simulation (Bao et al., 2020), but these studies were restricted to low-cycle fatigue (LCF) loads.

Experiments have shown fractographic details that the hypothesis that plastic deformation in localized shear bands is a precursor to initial cracking (James et al., 2013). The plasticity of amorphous polymers has been experimentally (macroscopically) measured by the yield strain observed prior to strain softening (Anand and Ames, 2006; Barriere et al., 2019; Jiang et al., 2015). The models capable of governing the macroyielding and development of viscoplastic deformation (i.e., the models suitable for investigating macroscopic structures) can be categorized as follows: [A] models in which the microstructure is replaced by the isotropic intermolecular resistance (Boyce et al., 1988; Engqvist et al., 2016; Holopainen and Wallin, 2012), [B] models in which the microstructure is described by internal variables related to the free volume (loosely packed regions in the material) (Anand and Ames, 2006; Barriere et al., 2019; Jiang et al., 2015), and [C] models based on internal variables related to entanglement-based microstructures (Jiang et al., 2020; Wang et al., 2019). A promising model for the rate- and temperature-dependent macroyield behavior of amorphous polymers was recently proposed by Jiang et al. (Jiang et al., 2020) (group C) based on subentanglement (SE) and topological entanglement (TE) microstructures (see Fig. 4(b)). Micro-/nanostructural approaches based on the evolution of the free volume (Bowman et al., 2019) (group B) and on crazing (changes in the fibril/chain disentanglement) (Venkatesan and Basu, 2015) (group C) tend to explain the origin of plasticity through molecular dynamics simulation. Clearly, crazing is generated in regions of high void volume (Venkatesan and Basu, 2015), i.e., the void volume and initiation of plastic deformation through crazing are interconnected. Fatigue failure in amorphous polymer structure has also been shown to develop through the mechanism of cyclic fracturing of fibrils (Ravi Chandran, 2016), leading to accumulated void volume fraction and cracking (James et al., 2013).

The viscoelastic-viscoplastic model introduced in Barriere et al. (Barriere et al., 2019) has been shown to be accurate under various multiaxial, long-term cyclic loading processes (Barriere et al., 2020), and it was applied in this research. However, this model is also limited in that it underestimates the shear ratcheting strain, especially that prior to rupture. The model's rigidity in shear is due to the applied eight-chain model (Boyce et al., 1988), which has been shown to be rather rigid under shear loads (Boyce et al., 1995; Wu and Giessen, 1993). On this basis, an improvement of the model is proposed.

In addition to the plastically induced failure, material also shows a fatigue damage mechanism (James et al., 2013; Ravi Chandran, 2016). Modeling the fatigue resistance of amorphous polymers is still beyond the ability of the research community, and no main consensus can be found from the literature (Ravi Chandran, 2016). The majority of the research has concentrated on low-cycle fatigue (Krairi and Doghri, 2014; Lu et al., 2016), and regarding longer service lives and ratcheting, the research has been focused on uniaxial cyclic loadings (Barriere et al., 2019; Holopainen et al., 2017; Kanters et al., 2016; Krairi et al., 2019; Wang et al., 2016; Xi et al., 2015). The experimentation and modeling to detect crack growth in tiny zones (not applied at the macroscopic/component level) have also frequently been restricted to uniaxial loading conditions (Hughes et al., 2017; James et al., 2013; Ravi Chandran, 2016). Interestingly, according to the vast majority of fatigue data, the stress-life (S-N) curves and fatigue crack growth curves of polymers show similar shapes to those of metals regardless of their microstructure (Ravi Chandran, 2016).

A fundamental fatigue damage model for predicting service lives of polymers under different stress levels and modes was proposed in Barriere et al. (Barriere et al., 2020) (contrast to cycle-counting approaches, movement of the endurance surface and damage evolution are defined in terms of stress increments, not of stress cycles.). However, also this models lacks in that it cannot take the loading history into account and is therefore limited to low plastic loadings. On this basis, a unified fatigue model capable of predicting fatigue damage from the ultralow-cycle regime (fewer than one hundred cycles) to the high-cycle regime (more than 100,000 cycles) is proposed, and the capability of the model to simulate the tests is demonstrated. The entire model was programmed by using the Intel® Fortran application and was also used in a user-defined material subroutine (UMAT) in the Abaqus/implicit finite element program (Abaqus, 2014). For a comparison of the results, also the damage model introduced by Lemaitre and Chaboche (Lemaitre and

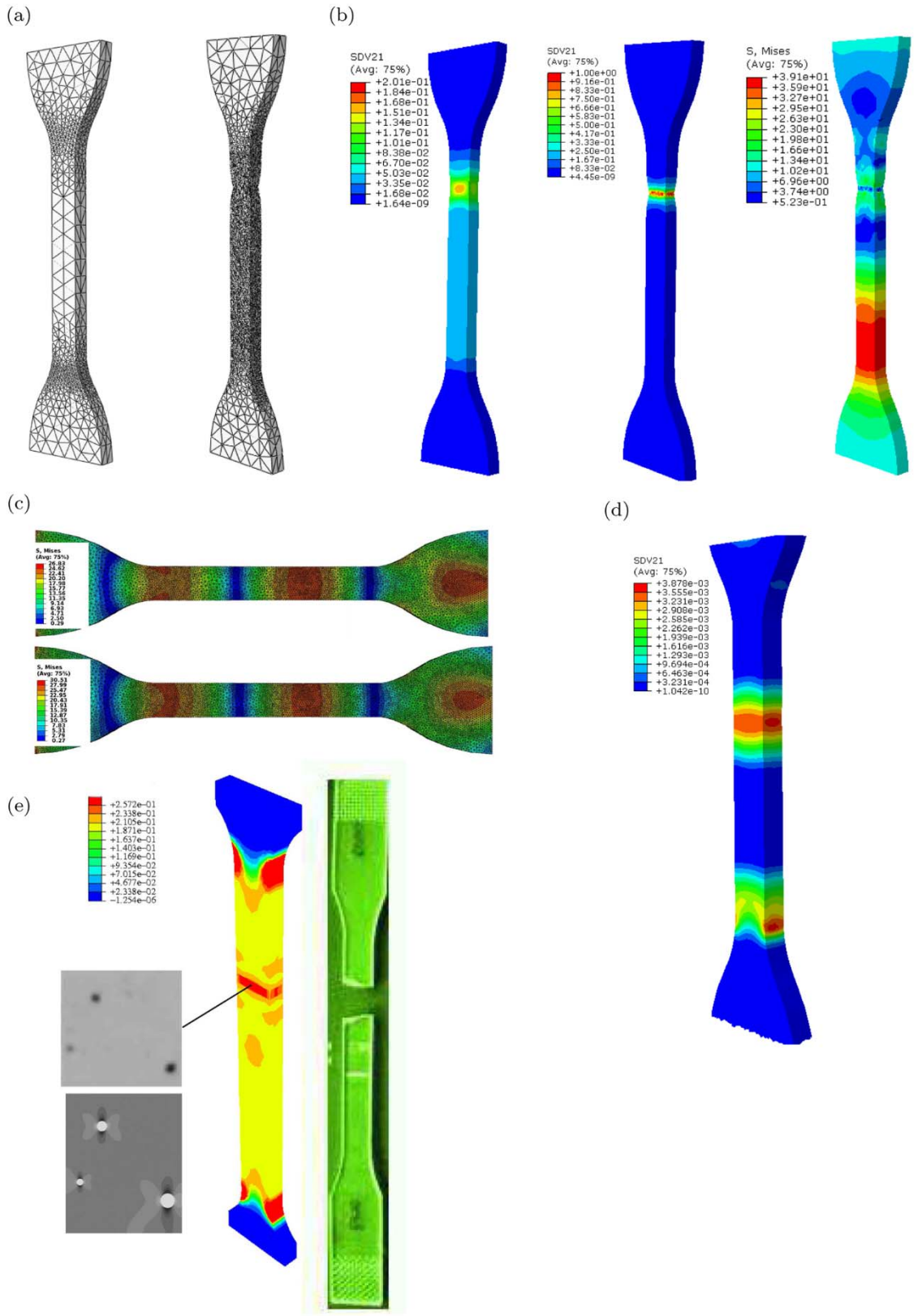

Fig. 1. Initial and final finite element meshes under monotonic loading (a). Distribution of damage and the von Mises stress (prior to rupture) based on the JC model and the Lemaitre-Chaboche model (Lemaitre and Chaboche, 1999) using remeshing (b). Increase in the von Mises stress under

cyclic loading at 100 and 500 cycles (c). Damage in the specimen's web at 500 cycles (d). Effect of impurities on the fatigue damage based on the Holopainen et al. model (Holopainen and Barriere, 2018) (e). Experimentally observed regions of impurities (grey/black regions in the upper inset) and calculated damage in the corresponding RVE (grey/black/white regions in the lower inset) and in the entire specimen at 100 cycles (red regions). The final rupture in the test specimen is also shown. (For interpretation of the references to color in this figure legend, the reader is referred to the web version of this article.)

Chaboche, 1999) (the $[1-D]$ concept) coupled with the established Johnson-Cook (JC) material model was implemented in the Abaqus.

The monotonic and cyclic tests covered uniaxial tension, torsion, and their multiaxial combinations. Based on the results of both testing and modeling, the influences of the mean stress, stress amplitude, loading rate, load path, and loading history on the cyclic deformation behavior (ratcheting) and service life are demonstrated, and the relationship between the model variables and microstructural changes is addressed.

2. Methods

2.1. Influence of geometrical and material imperfections

In addition to experimental observation (X-ray tomography and Werth video-check) of the defects of test specimens, simulations were utilized already at the beginning of the study to obtain test specimens without weaknesses. Consider first the simulated development of damage ($0 \leq D < 1$) in an imperfect test specimen. Analysis of entire structural components for long service lives requires a great deal of computational resources. Therefore, the analysis is done in practice using either a simple approach for the whole structure or an advanced approach only for the most stressed portion of the structure.

Considering first a simple approach for the entire specimen. The isotropic ductile damage model introduced by Lemaitre and Chaboche (Lemaitre and Chaboche, 1999) (the $[1-D]$ concept) was coupled with the well-known empirical viscoelastic-plastic Johnson-Cook (JC) material model (Abaqus, 2014), and the coupled model was implemented in Abaqus/Explicit (Abaqus, 2014; Cherouat et al., 2018). The adaptive remeshing procedure used by Cherouat et al. (Cherouat et al., 2018) was applied to polymers for the first time in this work. The remeshing was conducted with linear tetrahedra elements. The idea of remeshing is that the initially imperfect mesh is constantly updated to monitor the development of plastic deformation (crazing) zones based on the previously updated deformed mesh of the specimen. The updating of the mesh is based on an adaptive methodology implemented in the Optiform mesher package (Cherouat et al., 2018). When the damage variable D reaches its maximum (at integration points), the corresponding elastic modulus becomes zero, and the corresponding element is considered fully damaged and thus eliminated. A new boundary and new domain mesh are then generated. A small nonsymmetry in the initial element mesh, as shown in Fig. 1(a), reflects a small initial imperfection in the geometry or material of the specimen.

Consider a monotonic, static uniaxial tension increasing from zero to the rupture of an imperfect specimen at a strain of 0.14. The JC model parameters $E = 2100$ MPa, $\nu = 0.38$,$A = 40$ MPa, $B = 17$ MPa, $n = 0.42$ (plastic hardening), $C = 0.025$ (viscosity), and the damage model parameters $Y_0 = 0.0012$ MPa, $\gamma = 2.0$, and $\alpha = \beta = 1.0$ were fitted to this data. The corresponding parameter symbols are used in Cherouat et al. (2018). The development of damage and the von Mises stress distribution prior to rupture of the specimen is shown in Fig. 1(b). According to the $[1-D]$ modeling concept applied, the von Mises stress eventually vanishes in the most damaged region, implying that the material can no longer withstand the load.

Based on the same initial mesh as under the static load, a cyclic tension-compression loading (with a sinusoidal waveform) was also simulated; the stress ratio $R = -1$ (denoting the ratio between the smallest and largest stress), frequency $f = 5$ Hz, and the maximum stress of 24.3 MPa were used. The von Mises stress first increases in certain regions, as shown in Fig. 1(c), and ultimately vanishes due to the fully developed damage, which development is similar to that observed under the static load.

Although the applied model with the remeshing concept (Cherouat et al., 2018) is robust, it seems to overestimate service life; when extrapolating damage based on the development during 500 cycles (Fig. 1(d)), the service life attains the value of 60,000 cycles, while the measured service lives, although observed for $R = 0.1$ (tensile ratcheting), correspond to approximately 20,000 cycles. Hence, the damage development is sensitive to initial imperfections and is localized around them. Therefore, particular attention has been paid to test specimen quality, the matter of which is discussed below. Moreover, the JC constitutive model and the damage model used are purely empirical and do not include the specific features of amorphous microstructure observed under various long-term loading conditions.

Considering next a microstructural based approach for the most stressed portion of the specimen. The failure of amorphous polymers is closely interconnected to their microstructure and is due to the nucleation of microdefects or inhomogeneities, which result in considerable local inelastic deformations (Lugo et al., 2014; Poulsen et al., 2005; Ravi Chandran, 2016). Based on the micromechanically-based viscoelastic-plastic constitutive model and the fatigue damage model (Holopainen and Barriere, 2018), the influence of such inhomogeneities on fatigue damage in a representative volume element (RVE) is shown in Fig. 1(e) (simulated by Abaqus/implicit (Abaqus, 2014)). The mesh consisted of linear hexahedra elements. A load frequency of $f = 5$ Hz, a maximum stress of 97% of the peak yield stress (60 MPa, the highest stress observed before softening under displacement-control (Dreistadt et al., 2009)), and a stress ratio $R = 0.1$ (sinusoidal waveform) were applied. First, the fatigue damage was calculated for the entire specimen. Then, the applied load along the top region and the right lateral side of RVE was taken from an analysis of the entire specimen (Holopainen and Barriere, 2018). The focus of this study was the surrounding PC, i.e., the fatigue damage of inhomogeneities was not taken into

consideration and they were considered to be elastic. The finite element simulation of the RVE demonstrates that damage evolves in the vicinity of the inhomogeneities and attains its threshold for crack opening therein, while the majority of the material does not appear to be as much damaged. This finding conforms to our experimental observations in that the macroscopic ratcheting deformations show a rapid increase only when majority (90%) of the fatigue life (service life determined based solely on the fatigue failure) has been attained. Therefore, damage does not notably influence the macroscopic stress response during the fatigue life, i.e., fatigue damage and stress can be considered uncoupled, cf. (Holopainen and Barriere, 2018).

The predicted fatigue life becomes about 500 cycles which is rather close to the measured life, almost 600 cycles. However, the applied fatigue damage model results in an almost linear development of damage up to rupture (Holopainen and Barriere, 2018), which is quite unrealistic. The model is also based on a phenomenal description of viscoelasticity, unrelated to amorphous microstructural changes, and the plastic evolution law (Boyce et al., 1988), which is quite inaccurate for predicting the transient yield peak and thus the shape of the strain loops under cyclic loads (Anand and Ames, 2006; Barriere et al., 2019). Therefore, a more sophisticated model is proposed based on microstructural changes, and this model is discussed below.

2.2. Manufacturing of specimens

A thermoplastic mold with specific die cavities (based on ASME standard) was manufactured for the tensile and torsion test

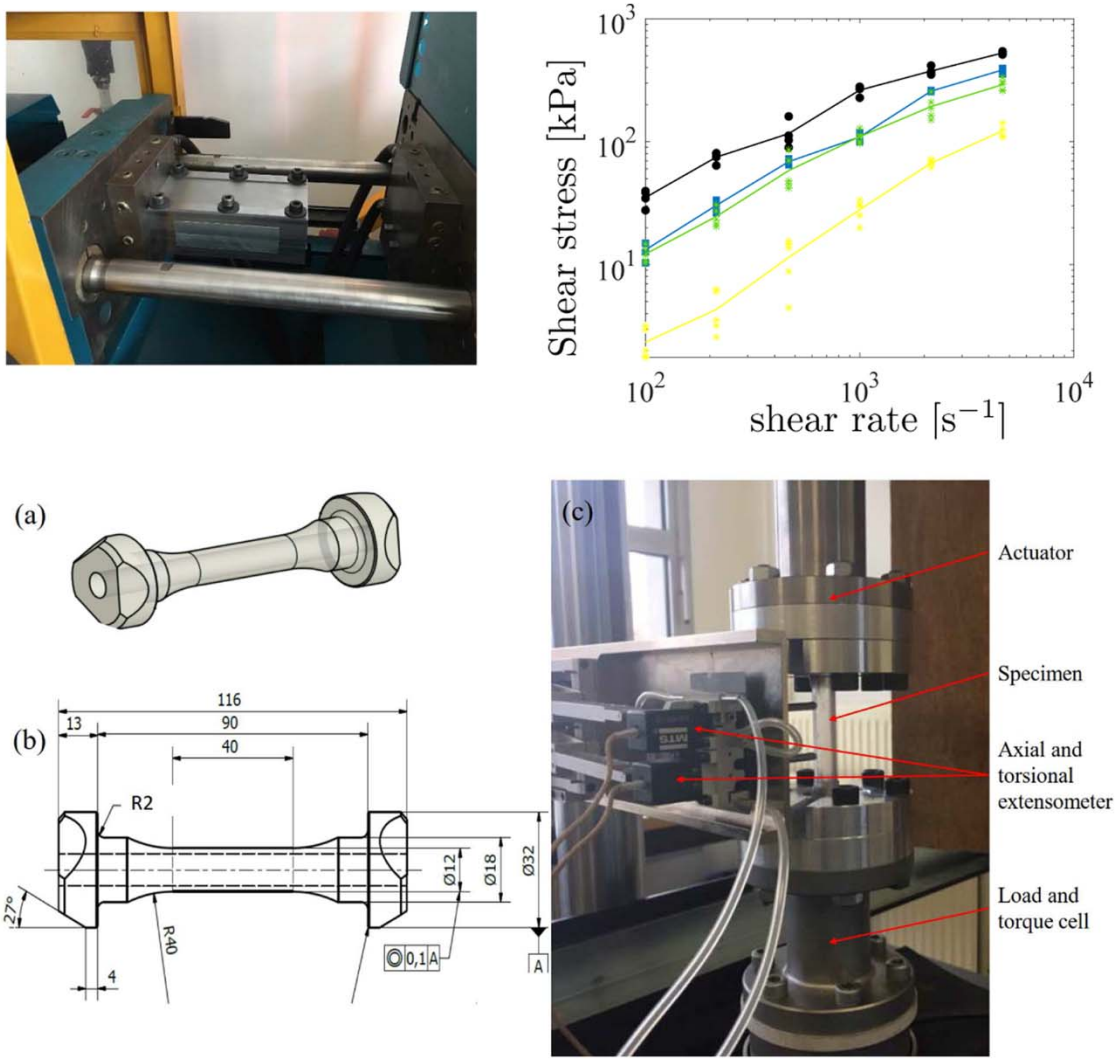

Fig. 2. Injection molding press equipped with a torsion test specimen mold (with a 22 mm screw diameter, 30.4 cm^3 maximal injection volume, 160 MPa maximal injection pressure, and 450 °C maximal injection temperature) (top left). The injection unit is on the right side. Shear rate vs. shear stress and temperature for dry PC: 260 °C (black), 280 °C (blue), 300 °C (green), 320 °C (yellow) (top right). Design (a) and dimension (mm) (b) of the torsion specimen. The testing setup (c). (For interpretation of the references to color in this figure legend, the reader is referred to the web version of this article.)

specimens (see Fig. 2, top left). The injection tests were realized with a dry polycarbonate (Lexan® 223R granulate, with a density of 1.2 g/cm^3, was provided by Sabic) held at 130 °C for four hours. The mold temperature was controlled by a water cooling/heating system from the ambient temperature to the mold temperature. The mold was maintained at 80 °C during the injection. The injection temperature comprised of the three heating zones of the injection nozzle (entrance 305 °C, middle 300 °C, and injection 295 °C). The injection pressure was set to 65 MPa. The specimens were cooled at ambient temperature.

The shear rate vs. shear stress and temperature from 260 °C to 320 °C, which responses describe the polymers' capability for injection molding, were measured using a standard capillary rheometer with a die cavity of 1 mm in diameter and 16 mm in length, see Fig. 2(top right). The so-called pseudoplastic behavior was observed, and to product test specimens without significant external defects, the runner and gate size of the mold were increased. It can be concluded that the PC applied is prone to temperature and thus is rather challenging to inject. However, after the said improvements were made, a large set of torsional and tensile tests specimens (over one hundred) were manufactured without significant external defects. Using differential scanning calorimetry (DSC), it was also verified that the injected specimens had the same physical properties as the granulate.

The geometry of the injection-molded tensile specimens is demonstrated in Fig. 1(top) in compliance with the standard (type IV specimen) (ASTM, 2003). A more detailed account of the geometry is given in Barriere et al. (Barriere et al., 2020). The geometry of the torsional specimens was determined according to the standard (ASTM, 2002) and is shown in Fig. 2(a-b). This specimen geometry, with the smaller inner diameter of 9 mm, was used to prevent untimely buckling under torsion. Because the test results are susceptible to flaws in the specimens, particular attention was paid to the quality of the specimens. The flaws were analyzed with X-ray tomography and Werth video-check. The high quality of the final shape was further verified by employing optic 3D metrology (Alicona analyzer). The confirmed surface faults were under 0.03 mm. The effect of the faults on the test results can be interpreted to be infinitesimal because the inaccuracies they caused in the cross-section and outer radius (6 mm) of the gauge section are only 1.1% and 0.5%, respectively.

2.3. Tension tests

The tests were conducted by employing an Instron® Electropulse E10000 machine having a displacement capacity of ± 30 mm and a load capacity of 10 kN:

- Displacement-controlled quasi-static tests at the strain rates of $\dot{\epsilon} = 0.001$, 0.01, and 0.1 s^{-1} until rupture;
- Cyclic force-controlled tests at $f = 5$ Hz (sinusoidal) until rupture at $R = 0.1$ and 0.5. The maximum stress values were 37.5, 50, 75, 90, and 97% of the peak yield stress, 60 MPa.
- Cyclic force-controlled two-step tests at $R = 0.1$ and $f = 5$ Hz applying two different consecutive load spectra with maximum stress levels of 54 MPa and 30 MPa and vice versa.

The first test set was designed to observe the tensile yield strain and stress, the peak yield stress and the corresponding strain, and softening at large strains. Representative stress vs. strain curves are given in the preceding study (Barriere et al., 2020). The elastic modulus becomes $E = 2100$ MPa (strain $\epsilon = 0.02$ and stress $\sigma = 42$ MPa), and the peak yield stress and strain vary between 60…63

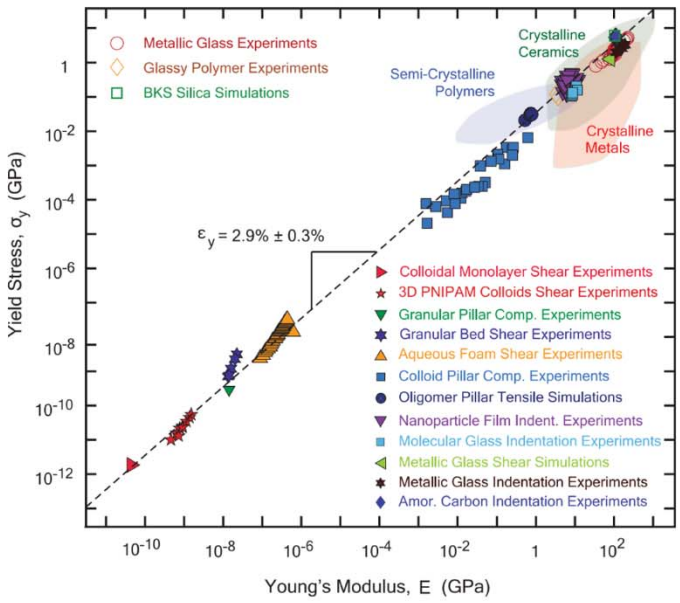

Fig. 3. The Ashby chart for the relation between the yield stress and Young's modulus of different materials (Cubuk et al., 2017).

MPa and 0.05…0.07 depending on the strain rate. The value of E complies with the Ashby chart shown in Fig. 3, indicating the relation between the yield stress σ_y and the Young's modulus E: $\sigma_y = E\epsilon_y = E(0.029 - 0.003) = 54$ MPa (Cubuk et al., 2017). The second test set was designed to study the effect of the mean stress and the stress amplitude on the ratcheting deformation and service life. The last test set was used to investigate the influence of loading histories on the remaining service life. The force F and the corresponding axial elongation u were recorded by the testing machine. In addition, the axial elongation was measured by an extensometer, as detailed in Table 1, and the results of the machine and extensometer were similar. The extensometer, glued onto the surface of the specimens to avoid slipping, was capable of all the tests up to the breakage of the specimens. The strain was calculated as $\epsilon := u/L$, where L is the gauge length of the extensometer applied. The nominal stress $\sigma := F/A$ has been chosen because it is easy to measure and calculate: measured force F divided by the original cross-sectional area A. The error in relation to the true Cauchy stress is small because the cyclic strains are relatively small (less than 10% as is depicted in Fig. 7.). Measurements of the cross-sectional area before and after the tests further showed that the change in the area remains small.

2.4. Torsion tests

The load cell capacity and the maximum angle of the testing machine applied were ±100 Nm and 135°, respectively. The following tests using force control were conducted:

- Quasi-static torsional tests using the torque speed 1 Nms^{-1} until rupture;
- Cyclic tests at $f = 1$ Hz (sinusoidal) and $R = 0.1$ until rupture when the maximum shear stress values were 30%, 50%, 65%, 75%, 82.5%, and 90% of the ultimate shear strength, 40 MPa.

The first test set enabled the ultimate shear strain and strength to be evaluated. Representative stress vs. strain curves are given in the preceding study (Barriere et al., 2020). Despite the standard applied (ASTM, 2002) is aimed at metals, the dimensions of the specimen and conventions were directly adjustable for polymers and the testing machine used. In addition, the torsion angle was

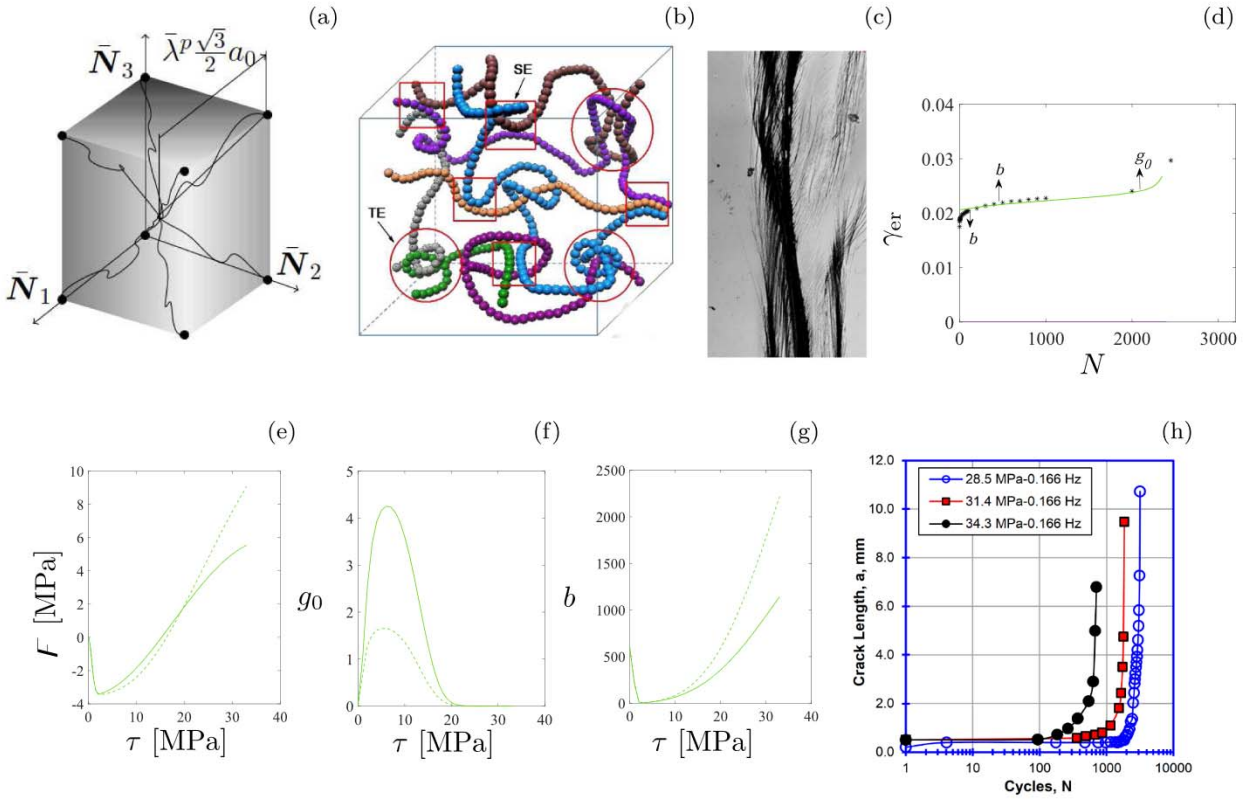

Fig. 4. Idealized chain network structure according to the 8-chain model (Boyce et al., 1988) (a) and to the Jiang et al. model (Jiang et al., 2020) (b). The base vectors $\bar{N}_{1,2,3}$ are the principal directions of the plastic deformation, the dimension of the undeformed element is a_0, and $\bar{\lambda}^p$ denotes the plastic chain stretch (Holopainen and Barriere, 2018). A 3D confocal laser scanning microscopy surface image showing bundles of joined shear bands (James et al., 2013) (c). The width of the region is about 200 μm. Initial proposal for f (dashed), the inspected values (circle), and the final smooth curve according to (3) (solid) (d). Effects of g_0 and b (demonstrated by the arrows that indicate an increase in g_0 and b) on the shear ratcheting strain (e). Growth of the fatigue crack length in PC single-edge notched tension (SENT) specimens (Ravi Chandran, 2016) (f).

Table 1
Details regarding the test equipment.

Test	ASTM-standard	Extensometer	Capacity of extensometer	Data acquisition (Hz)
Monotonic tension	D638-03	Instron 2620.601	5 mm, i.e., 20% strain	20
Creep and recovery	D2990-01	Instron 2620.601	5 mm, i.e., 20% strain	1
Cyclic tension	D2990-01†	Instron 2620.601	5 mm, i.e., 20% strain	1000
Monotonic torsion	E2207	MTS 632.68F	12°, i.e., 3% shear strain	15
Cyclic torsion	E2207	MTS 632.68F	12°, i.e., 3% shear strain	200
Cyclic tension-torsion	E2207†	MTS 632.68F	2.5 mm, i.e., 10% strain; 12°, i.e., 3% shear strain	10

† Not applied to the loading.

measured by the extensometer presented in Table 1. The extensometer was securely glued onto the surface of the specimens to avoid slipping. The shear strain and stress were defined as: $\gamma = d_o\theta/2L_g$ and $\tau = 16T/\pi(d_o^2 - d_i^2)(d_o + d_i)$, where θ is the angle in radians, T denotes the torque, $d_o = 12$ mm and $d_i = 9$ mm are the outer and inner diameters, respectively, and $L_g = 40$ mm is the gauge length of the specimens.

2.5. Combined tension and torsion tests

This test set was conducted to investigate the influences of different multiaxial load paths on the ratcheting deformation and service life of amorphous polymers. The different load-controlled load paths are depicted in Fig. 9. The duration of each cycle was 20 s, i.e., the frequency of 0.05 Hz was applied. The applied standard, including the details of the tests, is given in Table 1. The torsional test specimens were used, and the axial force, axial elongation, torque, and torsion angle were recorded by the testing machine. The torsion angle and axial elongation were also measured by the extensometer. The axial stress was calculated as $\sigma = 4F/\pi(d_o^2 - d_i^2)$.

2.6. Errors

To ensure the reliability of the results, each test was performed at least twice. The closest test result to the mean curve is applied and shown in the following figures. Considering the primary and secondary cyclic creep stages under uniaxial tension and pure torsion, the maximum standard deviation (SD) 0.0004 and 0.0022 in the ratcheting strains were observed when the maximum stress level 75% of the ultimate tensile and shear strengths was applied. These SDs correspond to less than 2% and 6% of the measured ratcheting strains. Another data which differs the most from the used data is shown in Figs 7(b) (tension) and 7(f) (torsion). Furthermore, the maximum SD under multiaxial loads was observed when the butterfly-type load (maximum stress level 50%) was applied, see Fig. 11(f). The maximum SD before the tertiary creep stage is 0.001 which corresponds to less than 10% of the measured ratcheting strains. During the tertiary creep stage, error between the data and model prediction is larger. However, the errors can be considered low enough for the model development. Moreover, in all loading cases, no increasing trend of error could be observed during the primary and secondary creep.

Fig. 8 further shows that the deviation between the fatigue lives is generally small. The largest deviation appeared under tension when $R = 0.5$, see Table 2. The extreme variation is due to the maximum stress level used, which is almost equal to the tensile strength, 60 MPa. Under torsion, the deviation of the fatigue lives was observed the smallest (less than 10%), and only the closest test result to the mean curve is depicted for the clarity of the figure.

The subsequently proposed model for the simulation of the data per se is unique without variation of the results. However, the least-squares fittings to obtain the requisite model parameters result in some errors (performed by Matlab's Curve Fitting Toolbox™). This computation error in relation to data error in the model development is considered small. On the determination of this computation error, it is referred to the Numerical Recipes series (Press and Teukolsky, 2007, Chapter 15).

3. Modeling of amorphous polymer behavior

3.1. Improved prediction of plastic deformation

The microstructural-based BPA model (Boyce et al., 1988) and the Anand and Ames model (Anand and Ames, 2006) represent the two key state-of-the-art approaches for investigating macroscopical material domains and entire structures. These two models are both based on the distinguished Haward and Thackray model (Haward and Thackray, 1968), which has been supplemented by a few

Table 2
Deviation of the measured fatigue lives under uniaxial tension ($R = 0.5$).

σ_{max} [MPa]:	59.4	58.2	54	45	30	22.5	15
SD/min(N) %:	67	< 1	10	< 1	22	8	< 1

internal state variables, enabling the prediction of large plastic deformations in three dimensions. Since the Anand and Ames model can accurately predict the transient yield peak that is typical of amorphous polymers (due to the change in local free volume characterizing the change in the internal state during yielding), this model was used as the basis of this research.

According to the thermodynamically correct Anand and Ames model, the evolution of plastic deformation is modeled by the following power-law type strain rate:

$$\dot{\gamma}^{vp} = \dot{v}_0 \left(\frac{\tau^{(1)}}{s^{(1)} - 1/3\alpha I_1} \right)^{1/m_0} \geq 0 \tag{1}$$

where $\dot{v}_0, m_0$, and α denote the material parameters, $s^{(1)}$ is an internal state variable (representing the molecular resistance to plastic shear flow (Anand and Ames, 2006)), $I_1 = \mathrm{tr}\,(\boldsymbol{\sigma} - \boldsymbol{\beta}) = \mathrm{tr}\,(\widetilde{\boldsymbol{\sigma}}) = \mathrm{tr}\,(\boldsymbol{\sigma})$ is the first invariant indicating pressure ($\boldsymbol{\beta}$ is the traceless deviatoric backstress (Anand and Ames, 2006; Barriere et al., 2019)), and $\tau^{(1)} = \sqrt{\mathrm{tr}\,(\widetilde{\boldsymbol{\sigma}}^2)/2}$ is the equivalent reduced stress. The notation tr denotes the tensor trace. Plastic deformation is suppressed under compression: micro-cracks are opened in tension and partially closed in compression (Anand and Ames, 2006; Cherouat et al., 2018). However, the plastic strain rate (1) has not been designated for torsion and multiaxial loads and is rather inaccurate under such load conditions (Barriere et al., 2020). Therefore, the following improved model is proposed (the changes are highlighted in green):

$$\dot{\gamma}_{\mathrm{ij}}^{\mathrm{vp}} = \dot{v}_0 \left(\frac{\tau^{(1)}}{s^{(1)} - 1/3\alpha I_1 + F\,(I_1, I_2; \alpha_k)} \right)^{1/\mathrm{m}_0} \geq 0 \tag{2}$$

where F is the function representing additional molecular resistance to plastic shear flow; α_k, where $k = 1 \ldots 8$, are material parameters (positive); and $I_2 = 1/2((\mathrm{tr}\,\widetilde{\boldsymbol{\sigma}})^2 - \mathrm{tr}\,(\widetilde{\boldsymbol{\sigma}}^2))$ is the second invariant. Based on the available experimental data, the two different values $\dot{\gamma}_{\mathrm{ii}}^{vp} = \dot{\gamma}_{\sigma}^{vp}$ for tension/compression and $\dot{\gamma}_{\mathrm{ij}}^{vp} = \dot{\gamma}_{\tau}^{vp}$ for shear $i \neq j$, where $i, j = 1, 2, 3$, are considered sufficient under multiaxial loads. The viscoplastic flow rule is given by $\boldsymbol{D}^{vp} = (\dot{\gamma}_{\sigma}^{vp}\widetilde{\boldsymbol{\sigma}}_{\sigma}/\tau^{(1)} + \dot{\gamma}_{\tau}^{vp}\widetilde{\boldsymbol{\sigma}}_{\tau}/\tau^{(1)})/2$, where $\widetilde{\boldsymbol{\sigma}}_{\sigma}$ and $\widetilde{\boldsymbol{\sigma}}_{\tau}$ include the diagonal and non-diagonal components of $\widetilde{\boldsymbol{\sigma}}$ (Barriere et al., 2019). The equivalent rate of the plastic deformation for the evolution of the internal, scalar variables $s^{(1)}$ in (1) and φ (free volume) (Barriere et al., 2019) is given by $\dot{\gamma}^{vp} = \sqrt{2\,\mathrm{tr}\,((\boldsymbol{D}^{vp})^2)}$.

The function F targets at improving the accuracy of evolution of the plastic deformation in (2) under different stress levels and modes. The required form of F was found to be quite complex and, after trial and error, the initial values of F were found from the fittings to the measured ratcheting strains under torsion, see Fig. 4(d). Then, the function was split into the two parts $F = F_1 + F_2$ representing relaxation away from the initial state (generated during the manufacturing process, and the fatigue loading is small enough to return the initial state after unloading) and growth, respectively. The initial response of F from zero was modeled as

$$\frac{\mathrm{d}(F_1 + A)}{\mathrm{d}I_2} = -C(F_1 + A), \quad C > 0,$$

and the integration results in $\ln(F_1 + A) = -CI_2 + B$, where $A = F_{1,\min} + 1, F_{1,\min} = \mathrm{abs}(\min(F))$, is a parameter to keep the logarithm real. The parameters $B = \ln(F_{1,\min})$ and $C = B/I_{2,\min}$ are taken from the conditions $F_1(I_2 = 0) = 0$ and $F_1(I_2 = I_{2,\min}) = F_{1,\min}$. Finally,

$$F_1 = e^{-CI_2}\left(F_{1,\min} - e^{CI_2}F_{1,\min}\right)$$

when the transformation $F_1 \to F_1 + 1$ was used.

Based on the data, the development of F_2 after the relaxation stage was approximated by $F_2 = C_2 e^{-C_3 I_2} f(\bar{I}_2) - C_4$, where $f = I_2^2$ is a suitable estimate. The value of C_4 is obtained from the condition $F_{2,\min} = F_{1,\min}$ and the values of C_2 and C_3 from the conditions $\mathrm{d}F_2/\mathrm{d}I_2 = \delta > 0$, when $F_2 = F_{2,\min}$, and $F_2(I_2 = I_{2,\max}) = F_{2,\max}$. Choosing δ suitably, $C_3 = 0.005, C_4 = F_{1,\min}$, and $C_2 = \exp(C_3 I_{2,\max})(F_{2,\max} + C_4)/(-I_{2,\max}) = 3E-5$. Finally the expression

$$F = e^{-C_0 I_2}\left(-F_{\min}\left(1 - e^{-C_1 I_2}\right)\right)_{0 \leq I_2 \leq I_{2,\min}} + \left(C_2 e^{-C_3 I_2} I_2^2 - C_4\right)_{I_{2,\min} \leq I_2 \leq I_{2,\max}},$$

where $C_0 + C_1 = C, C_0 << C_1$ (an order of magnitude smaller), was found and is shown in Fig. 4(d) (dashed curve). The initial drop was observed mandatory to capture cyclic creep under torsion. However, this proposal for F is not smooth and includes $F_{\min}$ and $F_{\max}$ which are difficult to determine. Therefore, based on the initial F proposed, a smooth function

$$F = e^{-\alpha_1 \bar{I}_2}\left(-\alpha_7\left(1 - e^{-\bar{I}_2}\right)\right) + \alpha_8 e^{-\alpha_1 \bar{I}_2}\bar{I}_2,$$

(the term $-\alpha_7(1 - e^{-\bar{I}_2})$ is for the initial drop) was first determined for torsion and then it was enhanced for the combined torsion and tension (a function of both I_1 and I_2). The final form is

$$F = e^{-\alpha_1 \bar{I}_2}\left(\left(\alpha_{2,s} e^{\alpha_4 \bar{I}_1} I_2^2 - \alpha_{5,s}\right)\left(1 - e^{-\xi I_1^2 \bar{I}_2}\right) - \alpha_7\left(1 - e^{-\bar{I}_2}\right) + \alpha_8 \bar{I}_2\right). \tag{3}$$

It is assumed that $\bar{I}_1 = \sqrt{I_1^2}$ and $\bar{I}_2 = \sqrt{I_2^2}$ are better estimates than I_1 and I_2 under compression; the influence of I_1 in the denominator of (2) is considered enough. Under torsion, $I_2 = -(\tau - \beta_{12})^2 \approx -\tau^2$ (fatigue loads), and this approximately also holds under combined tension and torsion since then $I_2 = \sigma\beta_{11} - 3/4\beta_{11}^2 - (\tau - \beta_{12})^2$, and the backstress component β_{11} in relation to σ remains small under the relatively small strains (Holopainen, 2013), observed under ratcheting loads. The material parameters used are α_k, where $k = 1,4,7,8$. In addition, for $\dot{\gamma}_\sigma^{vp}$ (axial deformations, $s = 1 = \sigma$) and $\dot{\gamma}_\tau^{vp}$ (shear, $s = 2 = \tau$), defined above, the parameters $\alpha_{2,s}$ and $\alpha_{5,s}$, where $s = 1,2$, are different, i.e., the total number of parameters k becomes eight. The constant $\xi = 10^{-5}$ MPa^{-4} in the third term (in parenthesis) is a sufficiently small number for the function f to be smooth at small stresses.

The function f is demonstrated in Fig. 5(a). To improve predictions, f tends to restrain the evolution of plastic deformation (2) at high shear stresses and enhance it when the shear stress is low (f is lowered). The function f is a composition of five components, each with a targeted purpose. The magnitude of f, in the intermediate- to large stress region, is controlled by the first exponent function and the second term in the first parenthesis. The exponent function of I_1 for uniaxial loads and the quadratic function of I_2 for shear loads were observed to be the most relevant forms to predict data and the molecular resistance. The first exponent function limits the magnitude above all at high shear stress levels and therefore $\alpha_1 << \alpha_4$. The last linear term fine-tunes the growth of f. When a shear load increases from zero, f rapidly reduces to $\alpha_8\bar{I}_2 - \alpha_7$ ($\alpha_1\bar{I}_2$ and $\xi I_1^2\bar{I}_2$ are close to zero) representing the minimum additional molecular resistance to plastic shear flow.

When modeling cyclic torsion up to rupture, it was observed that the free volume φ is dominant, and the constant parameters g_0 and b, which are used in the preceding models to predict uniaxial deformation behavior (Anand and Ames, 2006; Barriere et al., 2019), are insufficient and thus are replaced by nonlinear functions. Therefore, the saturation value $\tilde{s}^{(1)}$ of the variable $s^{(1)}$ in (1) is modified to be

$$\tilde{s}^{(1)} = s_{sv}(1 + b(I_1, I_2; b_k)(\varphi_{sv} - \varphi(g_0(I_1, I_2; g_k))) > 0, \tag{4}$$

where s_{sv} and φ_{sv} are the original model parameters and b_k, where $k = 1,\ldots,4$, and g_k, where $k = 1\ldots6$ are additional parameters (determined from torsional and multiaxial tests). The evolution of the free volume is defined as (Barriere et al., 2019)

$$\dot{\varphi} = g_0\left(s^{(1)} / s_{cv} - 1\right)\dot{\gamma}^{vp} > 0,$$

where

$$g_0 = \left(e^{-g_1 I_2^2}\left((1 - g_2 I_1^2)\bar{I}_2 \Big/ g_3 - g_4\right) + g_5 e^{-\xi I_2^2}\right) \Big/ \left(1 + g_6 I_1^2 \bar{I}_2\right) > 0 \tag{5}$$

and g_k, where $k = 1,\ldots,6$, are material parameters. The constant $\xi = 10^{-5}$ MPa^{-4} is a sufficiently small number for the function g_0 to be smooth at small stresses. The function g_0 was determined based on the similar phases as for f. As shown in Fig. 5(b), the predicted rate of the development of free volume (described by the dominant function g_0) is at its highest at a relatively low shear stress, and it then rapidly reduces despite an increase in stress. Similar growth peak is not provided under uniaxial tension, when g_0 approaches the constant value $g_5 - g_4 > 0$ for adjusting softening (Anand and Ames, 2006; Barriere et al., 2019). The effect of g_0 on the shear ratcheting behavior is demonstrated in Fig. 4(e): the function g_0 controls primarily the deformation before rupture (tertiary cyclic creep). From the view of the polymeric microstructure, the function g_0 limits the free volume, and thereby captures the highly nonlinear behavior of finite chain extensibility, i.e., entropically constrained stretching affected by the plastic deformation.

The first exponent function and the term $\bar{I}_2/g_3$ in (5) controls the magnitude of g_0, evolution of the free volume, and consequently, the saturation value (4) and the variable $s^{(1)}$ which influences the plastic deformation according to (2). The lower the value of g_0, the greater is the saturation value and the variable $s^{(1)}$ restraining the plastic deformation according to (2). As mentioned above, the plastic

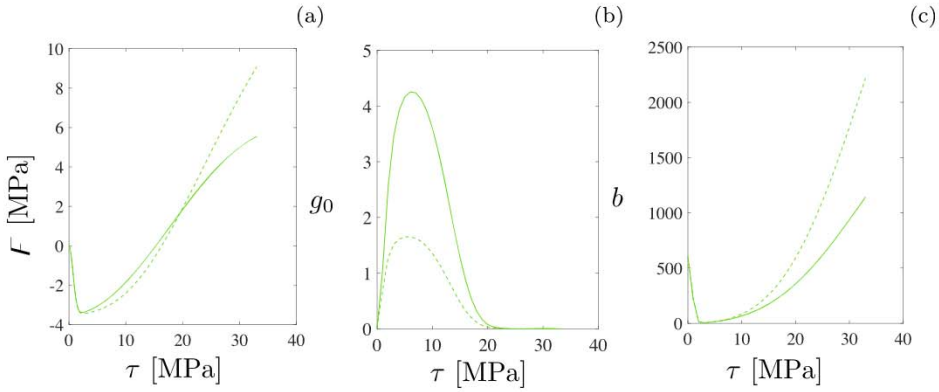

Fig. 5. Evolution of the proposed function f (a). Solid and dashed curves are for $\sigma = 0$ MPa and $\sigma = 10$ MPa (multiaxial load). Evolution of g_0 and b for the free volume (b and c). Solid and dashed curves are for $\sigma = 20$ MPa and $\sigma = 30$ MPa.The symbols σ and τ indicate the axial and shear stresses (Cauchy), respectively.

deformation is caused by crazing (changes in the fibril/chain disentanglement), i.e., the first component of g_0 describes stabilized crazing on average when the shear stress is high. The initial growth of g_0 at low shear stresses is lowered by the constant g_4 as well as it, under multiaxial loads, is reduced by the composition $(1-g_2\bar{I}_1^2)\bar{I}_2$, i.e. finite chain extensibility is reduced under multiaxial loads. The quadratic format of I_1 was observed the most relevant for capturing data and thus, the putative chain extensibility. The divisor in the parenthesis reduces the magnitude of g_0 in the intermediate- to large stress region as demonstrated in Fig. 5(b).

The effect of free volume on the molecular resistance and plastic deformation is further strengthened by the function b in (4) defined as

$$b = e^{-b_2\bar{I}_2}\left(1+b_3\bar{I}_1^2\bar{I}_2\right)\bar{I}_2\Big/\left(b_4+b_1e^{-\bar{I}_2}\right) > 0, \tag{6}$$

where $b_k, k = 1,\ldots,4$, are material parameters. The function b was determined based on the same phases as for f (similar shapes). Under uniaxial loads, $b = b_1$ (constant) adjusting the peak yield stress and softening (Anand and Ames, 2006). The function b is demonstrated in Fig. 5(c) and its effects on the ratcheting behavior are demonstrated in Fig. 4(e): the function b controls the primary and secondary creep. In accordance with the function f, the function b tends to restrain the evolution of plastic deformation (2) at high shear stresses (high b increases the saturation value (4) and the variable $s^{(1)}$) and enhance it when the shear stress is low. When a shear load increases from zero, b rapidly reduces to zero (by the last term) when $\tilde{s}^{(1)} = s_{sv}$ in (4) and the development of the plastic deformation resistance $s^{(1)}$ is suppressed. The growth of b under different stress combinations is controlled by the first exponent function and the second term in the parenthesis, where the quadratic formats of I_1 and I_2 were observed the most relevant for predicting data for the plastic deformation influenced by the free volume.

As is demonstrated in Fig. 5(a–c), the functions f, b, and g_0 approach the values used in the Anand and Ames model (Anand and Ames, 2006) as the shear stress decreases to zero (and $\dot{\gamma}_{ij}^{vp}$ in (2) approaches $\dot{\gamma}^{vp}$ in (1)). Thereby, the number of additional parameters needed in the functions f, b, and g_0 is reduced to 16. Although this number of parameters may seem large (original 18 + added 16 = 34), almost the same number is needed in the closest state-of-the-art models to model the uniaxial loading alone (Anand and Ames, 2006; Jiang et al., 2015; Krairi et al., 2019). Generally speaking, introducing additional parameters to an existing constitutive model makes the modified model more flexible. In addition, the proposed functions f (additional molecular resistance limiting the evolution of the plastic deformation), g_0 (evolution of the free volume), and b (influence of the free volume on the molecular resistance) are essential for modeling the measured cyclic plastic creep under different stress levels and modes. After trial and error, the proposed functions f, g_0, and b are essentially based on the exponent functions which are typically used to describe various natural phenomena such as creep and strain recovery after unloading (e.g., viscoelastic Maxwell and Kelvin-Voigt models) in solid mechanics (Sadd, 2018). A further discussion with connections to the polymer microstructure concerning the effect of the functions f, g_0, and b is given in Section 4.

3.2. Calibration of the viscoplastic model

The majority of the constitutive model parameters has already been used in the previous model (Barriere et al., 2019), and they all are given in Table 3 (the first 18 parameters were calibrated to one monotonic and one cyclic uniaxial data). Notably, the predicted

Table 3
Constitutive model and fatigue model parameters for the PC used.

Elastic and viscoelastic parameters									
Parameter	E	ν	$\dot{\nu}_0$	α	m_1	$s^{(2)}$	$c_A \times 10^{-6}$	$\mu_{A,sat}$	μ_A^0
Unit	MPa		s^{-1}			MPa	MPa	MPa	MPa
Value	2000	0.44	0.031	0.204	0.19	12	4.5	2500	8000
Viscoplastic parameters									
Parameter	s_0	m_0	C_R	N	h_0	b	g_0	s_{cv}	φ_{cv}
Unit	MPa		MPa		MPa			MPa	
Value	28.0	0.037	14.0	1.65	3500	600	0.014	26.5	0.0013
Parameter	$\alpha_1 \times 10^4$	$\alpha_{2,1} \times 10^9$	$\alpha_{2,2} \times 10^9$	α_4	$\alpha_{5,1}$	$\alpha_{5,2}$	α_7	α_8	$b_2 \times 10^4$
Unit	MPa^{-2}	MPa^{-3}	MPa^{-3}	MPa^{-1}	MPa	MPa	MPa	MPa^{-1}	MPa^{-2}
Value	7.7	13	1.8	0.6	2.0	1.0	3.5	0.015	7.0
Parameter	$b_3 \times 10^6$	b_4	$g_1 \times 10^5$	$g_2 \times 10^4$	g_3	g_4	g_5	$g_6 \times 10^4$	
Unit	MPa^{-4}	MPa^2	MPa^{-4}	MPa^{-2}	MPa^2			MPa^{-4}	
Value	7.0	1.8	2.6	3.0	0.65	0.346	0.36	7.0	
Fatigue model parameters									
Parameter	σ_0	a	C	$K \times 10^5$	L_1	L_2	ϑ	c	Q
Unit	MPa							MPa^{-1}	MPa^{-1}
Value	3.5	0.075	2.7	5.0	150	149	6000	0.03	0.0054
Parameter	$Q_b \times 10^4$	L_3	L_4	ϑ_2	$\mathscr{M} \times 10^{10}$	q			
Unit	MPa^{-2}	MPa	MPa	MPa					
Value	2.5	33	74	1600	1.2	2.45			

ratcheting strains are sensitive to the exponent parameter m_0, which is calibrated to one cyclic data for ratcheting deformation (Barriere et al., 2020). Under uniaxial loads, the functions g_0 and b approach the constant values $g_5 - g_4 > 0$ and $b = b_1$, respectively, determined from a monotonic uniaxial test. The greater the difference $g_5 - g_4$ and the value of b_1, the greater is softening (Anand and Ames, 2006).

The preliminary values of the additional parameters $\alpha_k, k = 1,4,7,8, \alpha_{2,s}$ and $\alpha_{5,s}, s = 1,2, g_k, k = 1,\ldots,4,6$, and $b_k, k = 2,\ldots,4$, were determined during the development of the improved model for the observed nonlinear torsional and multiaxial ratcheting. The parameters α_1, g_1, and b_2 are used to restrain the growth of the corresponding functions f, g_0, and b under large stresses, respectively, and the parameters $\alpha_{5,s}, \alpha_7, g_2$, and g_4 are then used to define their initial developments under small stresses. The remaining parameters $\alpha_{2,s}, \alpha_4, \alpha_8, g_3, g_6, b_3$, and b_4 are used to define the growth of the functions in the intermediate- to large stress region. Since the first exponent functions of f, g_0, and b limit the growth above all at high shear stress levels, it is required that $\alpha_1 << \alpha_4, g_1 << g_3$, and $b_2 << b_4$. It was also required that $\alpha_8 << \alpha_7$ and $\alpha_{2,s} << \alpha_{5,s}$ (to reach the minimum of f), $b_3 << b_4$ (to limit the growth of b), and also $g_2 << g_3$ and $g_2 << g_4$ for g_0 to be positive. The proposed functions have their minimum and maximum values. Considering pure shear or torsion (under multiaxial loads, examination of extreme values is more complicated and does not produce anything more that the parameters are positive). Then the derivative $\mathrm{d}f/\mathrm{d}\bar{I}_2$ is approximately

$$-\alpha_1 f + \alpha_8 \gtrapprox 0,$$

i.e., $f < \alpha_8/\alpha_1$. The minimum of b under shear loads is close to $\bar{I}_2/b_4$ and this value in $\mathrm{d}b/\mathrm{d}\bar{I}_2 = -b_2 b + 1/b_4 \gtrapprox 0$ ($b < 1/b_2 b_4$) yields $b_2 < 1/\bar{I}_2$. The maximum of g_0 under shear loads is approximately $e^{-g_1 \bar{I}_2^2}(\bar{I}_2/g_3 - g_4)$ and the derivative $\mathrm{d}g_0/\mathrm{d}\bar{I}_2$ is

$$-g_1 g_0 + e^{-g_1 \bar{I}_2^2} \Big/ g_3 \approx 0,$$

when finally $g_1(\bar{I}_2 - g_3 g_4) = g_1 \bar{I}_2 = 1$ ($\bar{I}_2 >> g_3 g_4$), i.e., $g_1 < 1/\bar{I}_2$. After few iterations, it was concluded that $g_1 < g_2 < g_6 < 0.001$ and $b_3 < b_2 < 0.001$.

As has been discussed in the preceding section, many parameters have a physical interpretation and meaning and they can be determined from targeted tests taking the proposed constraints into account. The final values of $\alpha_1, \alpha_7, \alpha_8, g_1, g_3, g_4, b_2$, and b_4 (eight parameters for shearing) were defined by least squares fitting of the targeted torsion data ($R = 0.1$) at different maximum stress levels of 30%, 50%, 75%, and 82.5% of the ultimate shear strength (40 MPa). The remaining eight parameters, $\alpha_{2,1}, \alpha_{2,2}, \alpha_4, \alpha_{5,1}, \alpha_{5,2}, g_2, g_6$, and b_3 for multiaxial loads, were fitted using least squares fitting to the data corresponding to combined tension and torsion (the squared and butterfly-type loads) when the maximum stresses were 30% and 50% of their strengths.

In summary, the number of additional parameters is 16, and their values were determined from eight tests. Based on the best understanding, the additional model parameters should be determined in the order just presented: first for torsion and then for multiaxial loads with the increasing stress levels. For the feasibility of the model in an industrial context, the possibility of using artificial intelligence in the calibration procedure would be of interest to study in future (Jung et al., 2020).

3.3. Improved prediction of the fatigue life

A unified fatigue model that is suitable for both high cycle fatigue (HCF) and LCF regimes under various loading modes is proposed here. This continuum-based fatigue model is an extension of the Ottosen et al. model (Ottosen et al., 2008) for HCF of metals, whose model is based on the concept of an evolving damage variable and an endurance surface moving in stress space. The center of the endurance surface is defined by the backstress quantity $\boldsymbol{\alpha}$. The prerequisite is the existence of an asymptotical extreme of lifetime, i.e., the endurance limit, and the fatigue under this limit is extinguished. The endurance limit of amorphous polymers is the threshold below under which no plasticity-controlled failure will occur (Pastukhov et al., 2020). As a result, the endurance limit does not depend on the processing conditions or the thermomechanical history and therefore can be used as a design parameter. Unlike in most important approaches for fatigue (cycle-counting and cumulative damage approaches), in this approach, the damage evolution and movement of the endurance surface are determined in terms of stress increments, not in terms of stress cycles (Frondelius et al., 2019; Ottosen et al., 2008). Therefore, this approach is well suitable for random 3D loadings.

To account for the loading history under plasticity-inducing loads and to simulate fatigue under torsion and multiaxial loads more accurately, the Ottosen et al. model (Ottosen et al., 2008) was modified. The endurance function (1) in Ottosen et al. model was replaced by (the changes are highlighted in green)

$$\beta = \frac{1}{\sigma_0}(\bar{\sigma} + g_{\mathrm{I}}(I_1; a, c) + g_{\mathrm{II}}(I_2; L_3, L_4, \vartheta_2) + g_{\mathrm{III}}(I_1, I_2; Q, Q_b) - \sigma_0), \tag{7}$$

where $\bar{\sigma}$ is the equivalent reduced stress (Barriere et al., 2020; Ottosen et al., 2008),

$$g \setminus tsb = a(1 - cI_1)I_1,$$

$$g_{\mathrm{II}} = L_3\zeta - L_4\left(\zeta + \frac{L_4}{\vartheta_2}\left(\exp\left(\frac{-\vartheta_2\zeta}{L_4}\right) - 1\right)\right), \quad \zeta = \sqrt{\bar{I}_2} \Big/ \tau_u, \text{ and}$$

$$g_{\mathrm{III}} = Q_b \bar{I}_1 I_2 - Q\bar{I}_2.$$

The invariants $I_1, I_2, \bar{I}_1$, and $\bar{I}_2$ were presented previously, and τ_u (40 MPa) is the ultimate shear strength. The original fatigue model parameters needed are σ_0 (endurance limit under the fully reversed load as $R = -1$ Ottosen et al. (2008)) and a (slope of the Haigh diagram as $R = -1$ Ottosen et al. (2008)). The additional parameters needed are c, Q, Q_b, L_3, L_4, and ϑ_2.

It is required that $\beta > 0$ when the damage evolves (Ottosen et al., 2008). In the endurance function (7), the linear relation aI_1 in the Ottosen et al. model (Ottosen et al., 2008) is replaced by the sum of the nonlinear functions $g_{\mathrm{I}}, g_{\mathrm{II}}$, and g_{III} to reduce β and thus, damage under heavy normal and shear stresses and under their combinations (LCF) respectively, see Fig. 6(a). The LCF damage in amorphous polymer structure has been shown to develop through the mechanism of cyclic fracturing of fibrils (Ravi Chandran, 2016), leading to accumulated void volume fraction and cracking (James et al., 2013). Therefore, on the microstructural basis, the proposed functions g_{I}, g_{II}, and g_{III} describe a reduced accumulation of the void volume fraction on average under different loading modes (LCF).

The first invariant I_1 in the function g_{I} reduces β and thus, fatigue damage under compression: micro-cracks are opened in a tensile state, whereas they are partially closed in a compressive state. The function g_{II} has the asymptote $L_3\zeta > 0$ as ζ is small (β and damage increase in the HCF region) and $(L_3 - L_4)\zeta < 0$ as ζ is large (LCF region, $L_3 < L_4$), see Fig. 6(a). The curvature ϑ_2 determines how rapidly the asymptote alters. A possible increasing effect of I_2 in g_{III} and β under mixed tension-compression is small ($Q_b << Q$). A comparison of the endurance functions according to the proposed model and the original fatigue model (Ottosen et al., 2008) is shown in Fig. 6(a) (before $\boldsymbol{\alpha}$ has been accumulated, being yet small in relation to the stress). It turns out that the endurance function β must be asymptotically reduced at high stresses (LCF region) to accurately reproduce the fatigue life. This feature is in line with the experimental observations, and the modified model encompasses a large range of mean stresses, as shown in Fig. 6(b).

The basis of improving the endurance function is the well-established Gerber's rule (1874) for metals, which is modified for polymers to be

$$\sigma_{\mathrm{a}} = \sigma_{-1}\left(1 - \zeta_1\left(\frac{\sigma_{\mathrm{m}}}{\sigma_{\mathrm{u}}}\right)^{\zeta_2}\right), \tag{8}$$

where σ_{u} is the peak yield stress (negative in compression). The parameters used are $\zeta_1 = 1.5$ and $\zeta_2 = 1.3$ (in the original Gerber's rule (1874), $\zeta_1 = 1.0$ and $\zeta_2 = 2.0$). The endurance surface $\beta = 0$ under uniaxial loads simplifies to $\sigma_{\mathrm{a}} = \sigma_{-1} - g_{\mathrm{I}} = \sigma_{-1} - a\sigma_{\mathrm{m}} + a_1(\sigma_{\mathrm{m}})^2$, cf. (Ottosen et al., 2008) (where $\sigma_{\mathrm{a}} = \sigma_{-1} - a\sigma_{\mathrm{m}}$), where $a_1 = ac$ and σ_{-1} is the fatigue strength as $R = -1$ (equals to σ_0 as fatigue stops generating). The comparison between this 1D endurance surface and Gerber's rule (8) shown in Fig. 6(b) reveals that they are close in tension, but the linear term $a\sigma_{\mathrm{m}}$ (aI_1 in three dimensions) is mandatory under compression to obtain sufficiently large fatigue strengths: it is assumed that the fatigue strengths under compression are considerably greater than those under tension. The endurance function (7) further includes the functions g_{II} and g_{III} for shear and multiaxial loads, respectively (they vanish under uniaxial loads).

Moreover, to include the loading history in the fatigue damage model in the LCF regime, the term

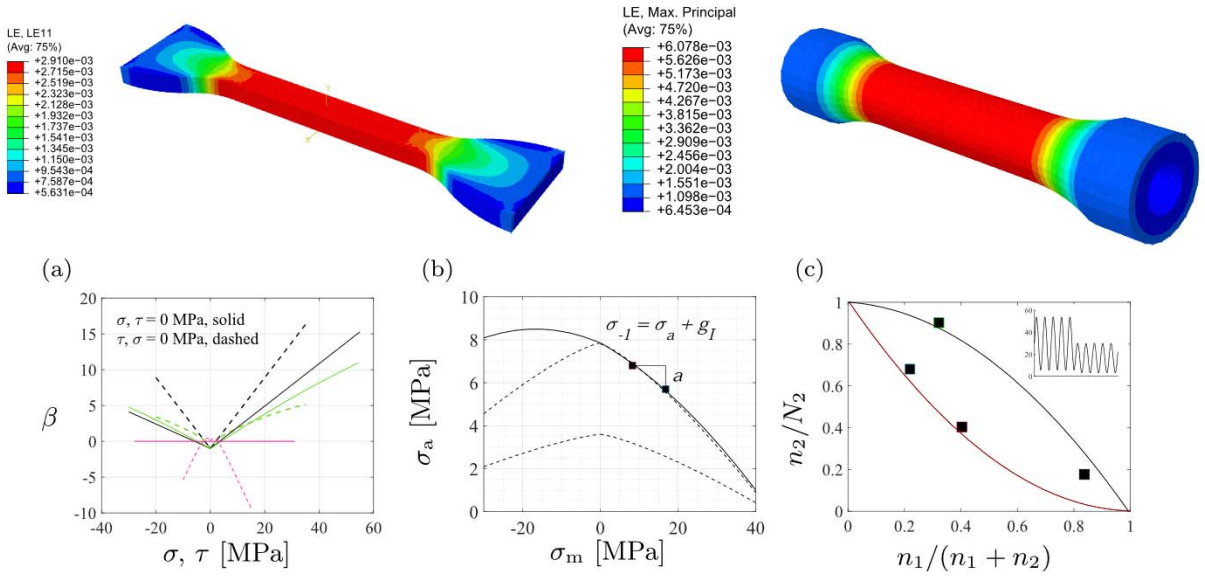

Fig. 6. Finite element simulations for tension and torsion (top). In the torsional specimen's web, pure shear prevails and thus, LE = LE12. Endurance function β according to the proposed model (green) and the original model (Ottosen et al., 2008) (black) (a). Function g_{II} (divided by the endurance limit σ_0) used in β is also shown (pink). Stress amplitude vs. mean stress (Haigh-diagram) for 60,000 cycles using the proposed model (black solid) and the modified Gerber's rule (8) (dashed) (b). Markers ■ denote the data points. In one dimension, $g_{\mathrm{I}}(\sigma_{\mathrm{m}}; a, a_1) = a\sigma_{\mathrm{m}} - a_1(\sigma_{\mathrm{m}})^2$. The Haigh-diagram for the endurance limit (dashed) by the modified Gerber's rule is also shown. Two-step loading (c). The inset presenting the lower curve shows the cyclic loading from high to low. (For interpretation of the references to color in this figure legend, the reader is referred to the web version of this article.)

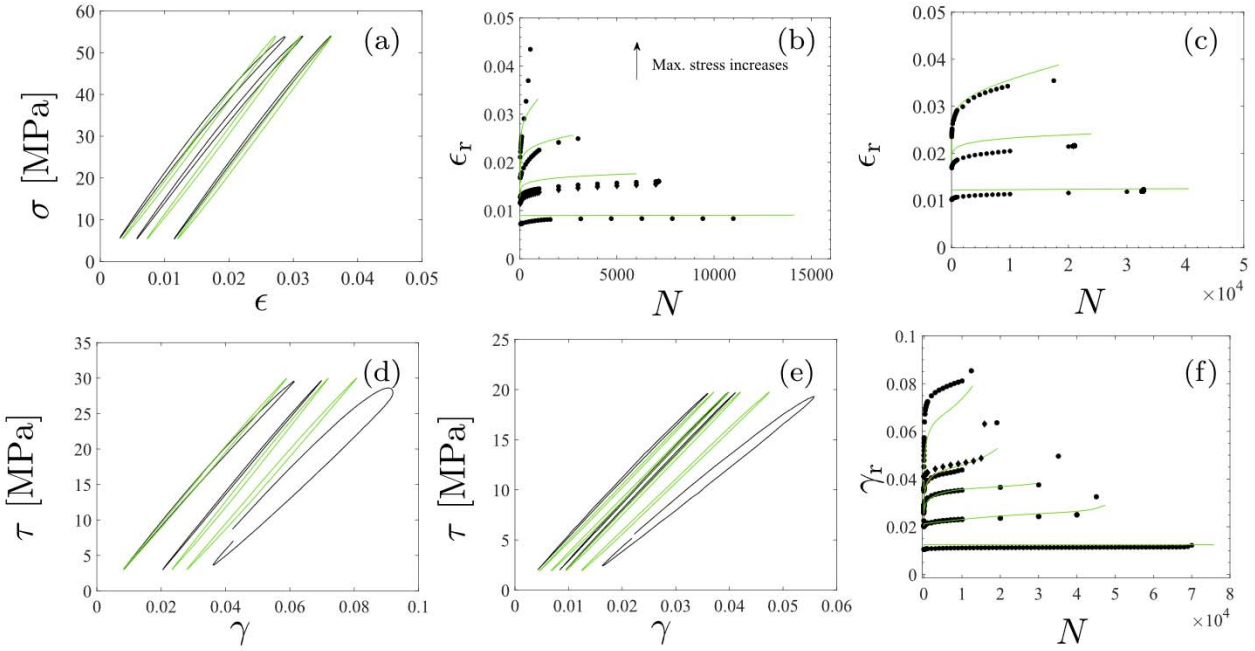

Fig. 7. The 30th, 300th, and 3000th loops under uniaxial tension when $f = 5$ Hz and $R = 0.1$ (a). The green and black colors mean the model results and data. Ratcheting strains (b). The markers • mean data. The maximum stresses used are 50%, 75%, 90%, and 97% of the peak yield stress, 60 MPa. Ratcheting strains when $f = 5$ Hz and $R = 0.5$ (c). The maximum stress levels are 50%, 75%, and 90%. Torsional test (black) and model (green) results for the maximum stress 75% of the ultimate shear strength ($f = 1$ Hz and $R = 0.1$) (d). The 30th, 10,000th, and 19,000 (before collapse of the specimen) cycles are shown. The loops for 50% (e). The 30th, 10,000th, 40,000th, and 49,100th (before collapse) cycles are shown. Shear ratcheting responses for the maximum stresses 82.5%, 75%, 65%, 50%, and 30% of the ultimate strength (f). The marker ♦ in figures (b) (tension) and (f) (torsion) indicates another data which differs the most from the used data.

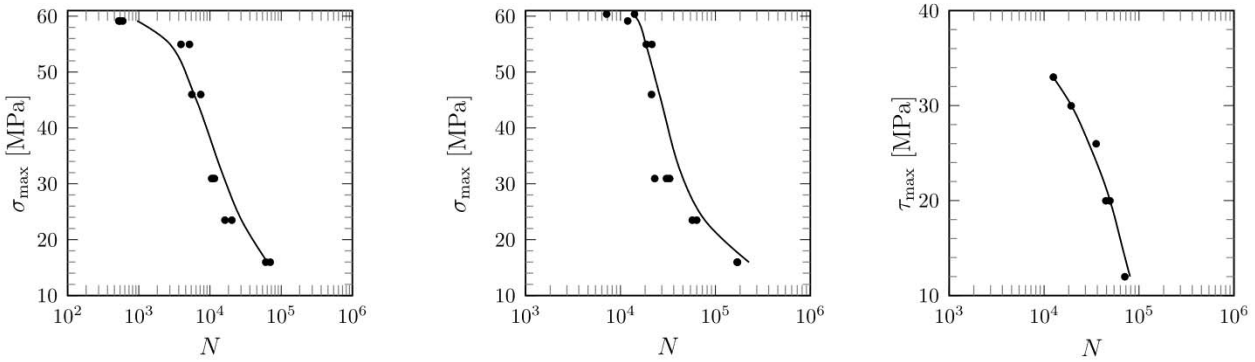

Fig. 8. Predicted uniaxial S-N curve and data points: $R = 0.1$ (left) and $R = 0.5$ (middle). Predicted torsional S-N curve and data points when $R = 0.1$ (right).

$$\dot{D}^{vp} = \mathscr{N}\frac{\mathrm{d}}{\mathrm{d}t}\left(\exp(\beta^q)\epsilon_{\mathrm{eff}}^{vep}\right) \geq 0 \tag{9}$$

with $\epsilon_{\mathrm{eff}}^{vep} := \int \dot{\epsilon}_{\mathrm{eff}}^{vep}\mathrm{d}t$ and $\dot{\epsilon}_{\mathrm{eff}}^{vep} = \sqrt{2/3\,\mathrm{tr}\left((\boldsymbol{D}^{vep})^2\right)}$, where q and $\mathscr{N}$ are material parameters, and $\boldsymbol{D}^{vep} = \boldsymbol{D}^{vp} + \boldsymbol{D}^{ve}$ ($\boldsymbol{D}^{ve}$ is the viscoelastic rate of the deformation (Barriere et al., 2019)), is added to the expression of damage evolution. It is assumed that the damage growth gradually increases with $\epsilon_{\mathrm{eff}}^{vep}$. If the trend is inverse (Praud et al., 2017), one can use $\ln(\epsilon_{\mathrm{eff}}^{vep})$ in (9). The $[1 - D]$ damage concept by Lemaitre and Chaboche (Lemaitre and Chaboche, 1999) is applied; i.e., the entire development of fatigue damage ($0 \leq D \leq 1$) is given by

$$\dot{D} = \dot{\bar{D}}\Big/(1 - D) + \dot{D}^{vp}, \quad \text{where } \dot{\bar{D}} = K\exp(f(\beta; L_1, L_2, \vartheta))\dot{\beta} \geq 0$$

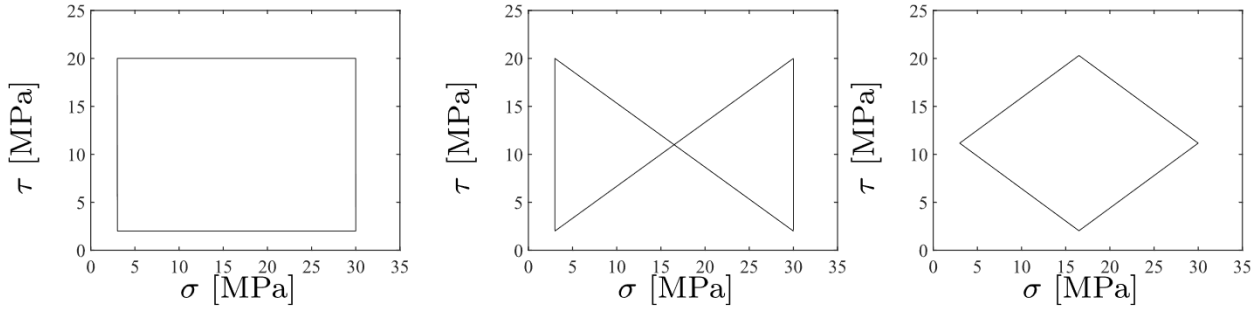

Fig. 9. Load paths applied in the load-controlled multiaxial tests. The symbols τ and σ denote the shear and axial stresses, respectively.

represents the LCF-HCF regime (excluding loading histories). The model parameters are K, L_1, L_2, ϑ, and the function f, extending the damage model to LCF regime, has been introduced in Barriere et al. (2020).

Numerical solution algorithm is discussed in Holopainen and Barriere (2018). As noted in the Section 2.1, the two systems of equations for the fatigue model and the constitutive model are regarded as uncoupled, i.e., fatigue damage D is calculated retrospectively.

3.4. Calibration of the fatigue model

Since the tensile specimens used are not aimed at compression, the initial values of the HCF parameters σ_0 and a (for the stress ratio $R = -1$) were determined from uniaxial tensile tests: the maximum stress at 25% of the peak yield stress $\sigma_u = 60$ MPa as $R = 0.1$ and the maximum stress at 37.5% as $R = 0.5$ (for both, $N \approx 60{,}000$). Moreover, a uniaxial test with a maximum stress of 37.5% ($N \approx 20{,}000, R = 0.1$) was used to define the remaining HCF parameters C, K, and L_1 applying least squares fitting, while σ_0 and a were slightly reduced. Then, the LCF parameters $\mathscr{N}, q, L_2$, and ϑ were fitted to the uniaxial test ($R = 0.1$) with a maximum stress of 90%, while C, K, and L_1 were yet slightly amplified. In the fourth stage, the parameter $c < a$ was extracted from the uniaxial test with the $R = 0.5$ and the maximum stress of 90%. Then, the parameter Q was adjusted to the torsion test where the maximum shear stress was 75% of the ultimate shear strength. Finally, the parameters Q_b, L_3, L_4, and ϑ_2 were extracted from data for the squared load paths with maximum stresses of 50% and 30% (defined below). It was required that $L_4 > L_3$ and $Q_b \ll Q$ to attain the asymptotes of g_{II} and g_{III}, respectively.

The total number of fatigue model parameters was 15, and their values were determined from eight tests. All the fatigue model parameters are given in Table 3. Although the number of parameters seems to be high, simpler empirical models (Lemaitre and Chaboche, 1999) cannot accurately reproduce fatigue lives from the LCF region to the HCF region under different loading modes owing to the complex ratcheting behavior arising from amorphous microstructure.

4. Results

Based on the proposed model, the distributions of axial strain (after 60 cycles when $\sigma = \sigma_{\min}, f = 5$ Hz, $R = 0.1$, and the maximum stress is 90% of the peak yield stress, 60 MPa) and shear strain (after 50 cycles when $\tau = \tau_{\min}, f = 1$ Hz, $R = 0.1$, and the maximum shear stress is 50% of the ultimate shear strength, 40 MPa) in high-quality tensile and torsion specimens without notable imperfections are shown in Fig. 6 (simulated by Abaqus/implicit). As can be assumed from the geometry of the specimens, as described by the standard ASTM D638 (ASTM, 2003), the responses in the specimens' gauge section or web are homogeneous. This outcome allows us to perform the forthcoming simulations in a single material (integration) point representative of the specimen's web. This is a significant advantage when modeling long service lives.

4.1. Plastic failure mechanism in amorphous structure

The applied concept of free volume in the material represents loosely packed regions around polymer chains with a reduced chain density at the nanoscale and microscale (Anand and Ames, 2006; Losi and Knauss, 1992). The concept of the free volume has been used to successfully describe several polymeric phenomena, such as anisotropic hardening at large strains and creep behavior (Anand and Ames, 2006; Bowman et al., 2019). An increase in the free volume has frequently been connected to the nucleation, growth, and coalescence of tiny voids on the polymer chain network (Bowman et al., 2019) and has been used to model damage (Francis et al., 2014). Therefore, the free volume has an asymptotical upper limit. The experiments processed by quenching (rapid cooling at an ambient temperature, as used in this research) show a greater amount of free volume compared to the experiments processed by slowly cooling specimens in a furnace (Anand and Ames, 2006). The growth of the free volume has been reported to be strongest at crack tips (e.g., around impurities) where crazing occurs and microscopic cracks initiate (Holopainen, 2014). The development of microcracks leads to the occurrence of shear bands, as illustrated in Fig. 4(c), and finally, through crazing, to the formation of macrocracks (James et al., 2013; Poulsen et al., 2005). The upper limit of the free volume is assumed to represent the initial formation of macrocracks, when the free volume is still low (Anand and Ames, 2006). The development of microcracks to macrocracks is illustrated in Fig. 4(f). This

accelerating crack growth explains the increasing (plastic) ratcheting deformation prior to rupture (tertiary cyclic creep) shown e.g., in Fig. 7(f).

As has been demonstrated in Fig. 5(b), the predicted development of the free volume (in terms of the dominant function g_0) under torsion shows that the weakest regions (initial plastic zones) in the material rapidly enlarge during loading, whereas the remaining packed regions take significantly more time to enlarge. Interestingly, this characteristic resembles the observed development of the void number density resulting in accumulated void volume (Bowman et al., 2019). The development of the free volume vs. microstructural changes is discussed below in the *Multiaxial loadings* section. Because the model is based on the stress invariants, the development of the free volume is similar under unloading, although in reverse. This is partly correct, assuming that the tightly packed regions partially reopen when the load is removed. Therefore, the development of the free volume is represented by its average during each cycle.

4.2. Tension results

Damage to a material restricts the service life and is known to be a function of the stress history. Consider the two different consecutive load spectra shown in Fig. 6(c). The internal state at the beginning of the second load spectrum depends not only on the present damage but also on the previous damage and the hardening state (Chaboche and Lesne, 1988). The two-step loading histories are described by the following numbers: n_1 and n_2 denote the number of load cycles of two different load spectra at the maximum stress levels of 54 MPa and 30 MPa ($R = 0.1, f = 5$ Hz) from high to low, and vice versa from low to high. The number n_1 represents the number of prestressing cycles and n_2 represents the number of cycles of remaining life. The number of cycles N_2 denotes the service life when solely the latter loading has been applied. The measured values of N_2 under the high and low loads are 4000–5000 and 11, 500–15,000 cycles, respectively. The proposed model is able to capture the observed service lives under the high-to-low and low-to-high loads well: the most presentative data points in Fig. 6(c) fall within the predicted ranges.

Fig. 7 (a) further shows hysteresis loops when the maximum stress is near to the peak yield stress of 60 MPa (close to the ultimate tensile strength observed under force-controlled tests). The hysteresis loops exhibit evident ratcheting strain (also termed cyclic creep) as the load ranges between its maximum and minimum values (Holopainen et al., 2017; Jiang et al., 2015; Kang and Kan, 2017). The ratcheting strain ϵ_r is defined as the mean value of the minimum strain ϵ_{min} and the maximum strain ϵ_{max} in each cycle. In the subsequent figures, the predictions end when full damage ($D = 1$) is reached. The best fits between the data and predictions based on the variations in the maximum and minimum stresses of the two percentages are presented.

Considering the ratcheting at the highest load level in Fig. 7(b), the experimental response quickly grows and becomes greater than the model response after 100 cycles. The intense growth of the measured ratcheting strain is owing to a mechanism of brittle failure, such as the scission of the polymer chains (Vernerey et al., 2018), not completely governed by the plasticity model and the fatigue damage model proposed. The applied high loading also results in the increase in temperature, affecting a small softening of the material. At the lower stresses, as demonstrated in Fig. 7(b, c), the model predicts the ratcheting strains and service lives accurately. The experimental and model results in Fig. 7(b, c) also reveal the following:

- ratcheting strain ϵ_r increases with amplitude and R (mean stress);
- ϵ_r increases with R and mean stress, even with a lower stress amplitude, even though
- ϵ_r increases with a higher stress amplitude as the maximum stress is approximately equal to the peak yield stress; and (at fixed maximum stress)
- the service life grows along with R.

The measured and predicted time-to-failure vs. maximum stress responses for uniaxial tension are shown in Fig. 8. It can be concluded that the proposed model accurately predicts short- to long-term ratcheting and service lives under different uniaxial loads.

4.3. Torsion results

The torsional ratcheting strain γ_r is defined as the mean value of the minimum and maximum shear strains γ_{min} and γ_{max}, respectively, in each cycle. First, consider the highest maximum stress level at 90% of the ultimate shear strength, 40 MPa. As with that under tension, the observed ratcheting strain exhibits a prompt increase, which behavior is caused by an abrupt material failure and a small rise in temperature, affecting softening. Due to this rapid failure, the test specimen broke at about 60 cycles, whereas the model shows a service life of 100 cycles.

Consider then the maximum stress levels of 75% and 50%. The predicted loops up to 10,000 cycles are similar to the experimental ones, as shown in Fig. 7(d, e). As failure starts to affect, the measured ratcheting strain increases, the stiffness of the material decreases, and the area of the hysteresis loops grows (indicating a drop in mechanical energy). The model cannot predict the last two characteristics since the stress and the fatigue damage are regarded as uncoupled, and consequently, on the microstructural basis, the predictions comply with permanent chain deformation rather than polymer chain breakage. On the other hand, as shown in Fig. 7(d, e), the chain breakage and the loss of mechanical energy actually commence once the majority of the service life (over 90%) has been passed. Although the shape of the predicted load cycles prior to rupture may differ from that observed, the model, however, accurately predicts the ratcheting strains and service lives, as shown in Figs. 7(f) and 8.

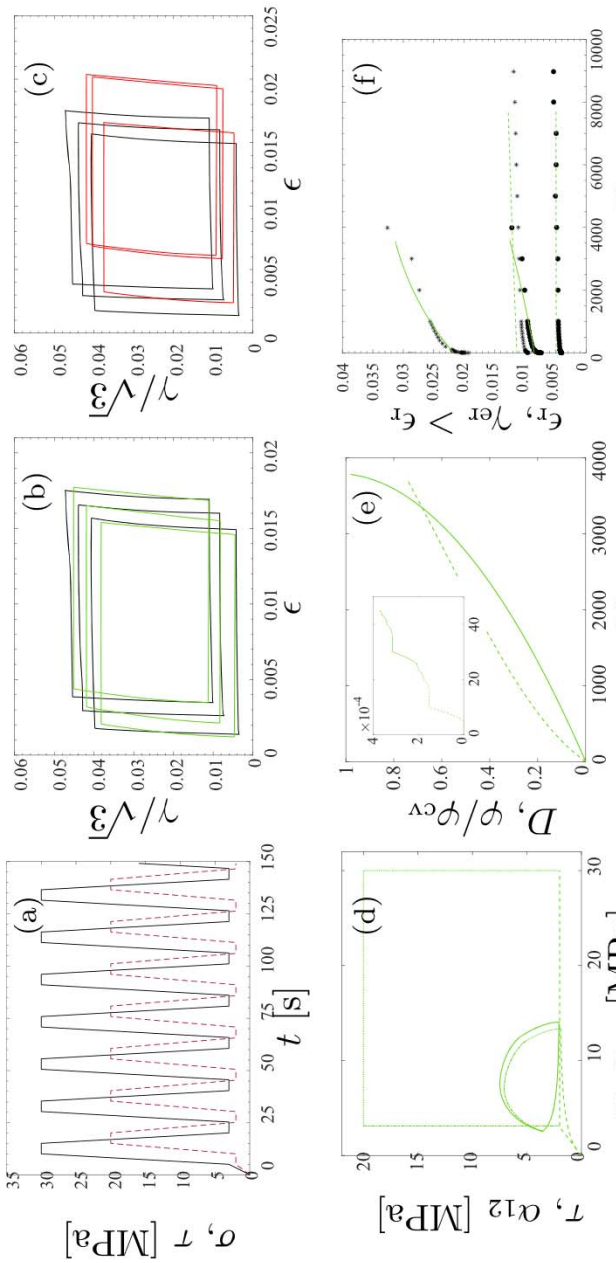

Fig. 10. Square-type load path (a). Shear and axial stresses are separated by the dashed and solid curves. The measured (black) and predicted (green) 100th, 1000th, and 3500th (90% of the service life) cycles when the maximum shear and axial stresses are 50% of their strengths (b). The same cycles predicted by the original model (red) based on the plastic evaluation rule (1) (c). Components of stresses and $\boldsymbol{\alpha}$ during the first cycle (d). The different loading phases are highlighted by the different line types. Development of fatigue damage D (solid) and free volume (dashed) (e). The inset shows D increasing during the first two cycles. Predicted shear and axial ratcheting strains when the maximum stress levels of 50% (solid) and 30% (dashed) are applied (f). The markers * and ● denote the corresponding data. (For interpretation of the references to color in this figure legend, the reader is referred to the web version of this article.)

4.4. Multiaxial loadings

To describe multiaxial loadings in one dimension, the equivalent stress and strain are defined as

$$\sigma_{\text{eqv}} := \sqrt{\sigma^2 + \left(\sqrt{3}\tau\right)^2} \text{ and } \epsilon_{\text{eqv}} := \sqrt{\epsilon^2 + \left(\gamma/\sqrt{3}\right)^2},$$

respectively (Lu et al., 2016). Additionally, the shear ratcheting strain γ_r defined above is replaced by the equivalent ratcheting strain $\gamma_{er} = \gamma_r/\sqrt{3}$.

The load paths applied are illustrated in Fig. 9. First addressing the details of the squared load path shown in Fig. 10(a), the strain responses in Fig. 10(c) reveal that the original model based on the plastic evolution rule by (1) underrates the shear strain and exaggerates the uniaxial strain. The predictions according to the improved rule (2) in Fig. 10(b) clearly evidence improvement in the model result. Due to the quite long-lasting holding time used (the duration of cycles is 20 s), the test also services to detect some static creep (at the maximum stresses) and recovery (at the minimum stresses). It is striking that neither the test results nor the model show marked creep or recovery under torsion, while they both are marked under tension. This result indicates that the amorphous polymer structure will resists creep and recovery under torsion (shear).

As shown in Fig. 10(d), the backstress $\boldsymbol{\alpha}$, that defines the center of the endurance surface in the model (Barriere et al., 2020; Ottosen et al., 2008), remains quite small in relation to the stresses that define the endurance surface. A similar result is also observed in certain aluminum alloys (Lindström et al., 2020). The corresponding developments of the free volume and fatigue damage D are shown in Fig. 10(e); it is the fatigue damage that finally determines the service/fatigue life. Despite the equally repeated cycles, the damage gradually increases which is due to the canonical $[1 - D]$ damage concept applied in this approach. This behavior is inherent to ductile materials and represents in amorphous polymers fracturing of fibrils leading to accumulated void volume fraction and cracking (James et al., 2013; Ravi Chandran, 2016).

The inset in Fig. 10(e) further shows that damage develops most intensively at the beginning of the load cycles, i.e., during tension, and is suppressed under torsion when $\boldsymbol{\alpha}$ (defining the center of the endurance surface) increases, cf., Fig. 10(d). The more rapid increase in damage under tension than that under torsion is also evident from the service lives shown in Fig. 8. When tension is reduced while torsion remains constant, $\boldsymbol{\alpha}$ continues to slightly increase, and damage again shows an increase. Finally, when torsion and eventually $\boldsymbol{\alpha}$ are reduced, the growth of damage tails off. Thus, the development of fatigue damage and the backstress $\boldsymbol{\alpha}$ (center of the endurance surface) are strongly influenced by the applied loading mode, and the amorphous structure seems to well resist fatigue damage under torsion.

When investigating butterfly-type loading, the macroscopically observed ratcheting strains increase the most during the first tens or hundreds of load cycles, depending on the maximum stress applied, cf. 11(c). This behavior represents the primary cyclic creep. Ratcheting deformation (especially shear) also shows a notable increase once 90% of the service life has been passed (tertiary cyclic creep), see Figs. 11(b-c) and 7(f) (torsion). It is likely that the free volume also increases most intensively during the primary and tertiary stages, see Fig. 10(e). Moreover, the impact of the fatigue damage is strongest at the end of the service life, i.e., during the tertiary stage, Fig. 10(e). The combined development of the free volume and fatigue damage (material failure), defined by $(D + \varphi/\varphi_{cv})/2$, resembles the development of the void volume accumulated by the void number density (Bowman et al., 2019). When the failure increases during load cycles, the volume of crazing (plastic) regions (corresponding to the void volume fraction) gradually increases. During the tertiary stage, the volume of crazing finally attains its threshold for the substantial material rupture and failure of the entire specimen.

On the microstructural basis, as has been mentioned in Section 3.3, the proposed fatigue model functions g_i, g_{II}, and g_{III} (under different loading modes) for the reduction of the endurance function and fatigue damage describe a reduced accumulation of the void volume fraction under heavy loadings (LCF). It was also mentioned in Section 4.1 that the function g_0 describes the observed, reduced

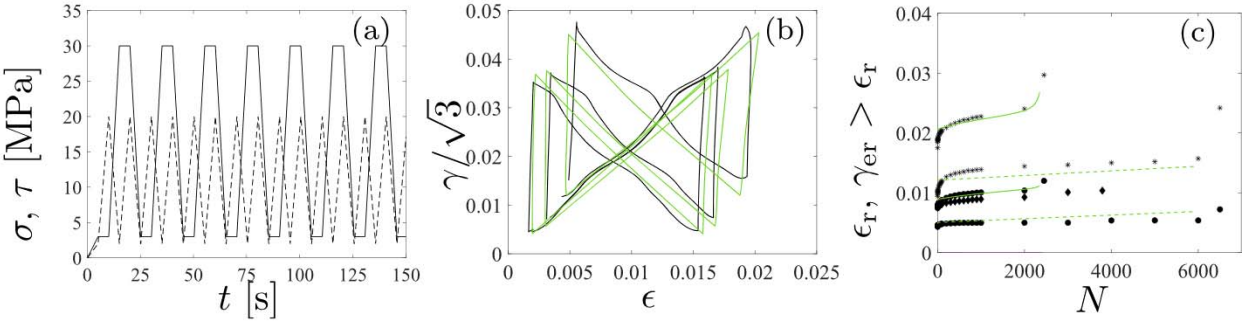

Fig. 11. Butterfly-type load path (a). Shear and axial stresses are separated by the dashed and solid curves. Measured (black) and predicted (green) axial strain vs. shear strain when the maximum stresses are 50% of their strengths (b). The 100th, 1000th, and 2400th (just prior to rupture) cycles are demonstrated. Predicted shear and axial ratcheting strain responses when the maximum stress levels are 50% (solid) and 30% (dashed) (c). The markers * and • denote the corresponding data. The symbol ♦ indicates another data which differs the most from the used data. (For interpretation of the references to color in this figure legend, the reader is referred to the web version of this article.)

development of the void number density and the void volume fraction under heavy loadings. Furthermore, the plastic deformation, through crazing, is generated in regions of high void volume (Venkatesan and Basu, 2015), i.e., the proposed constitutive model function g_0 and the proposed fatigue model functions all tend to describe the reduced development of the free volume and plastic deformation (which is also influenced by the proposed functions f and b) in the LCF region.

4.5. Comparison of the load paths

In all load cases, both the predictions and data show rapidly increasing initial ratcheting strains (primary cyclic creep), which then progressively reach their stabilized values (secondary cyclic creep) after quite a small number of cycles. Among the three different multiaxial loadings applied, the butterfly-type load path results in the most intense increase in ratcheting deformation prior to rupture, i.e., tertiary cyclic creep seems to be enhanced under combined tension and torsion when torsion in relation to the axial stress remains relatively small during the load cycles. In the model, the tertiary cyclic creep in torsion increases with the function g_0 for the rate of the free volume, i.e., the free volume (and void volume) significantly affects the shear ratcheting strain prior to rupture. Preliminary tests with imperfect torsion test specimens, including internal flaws and a larger void volume observed by the X-ray tomography, similarly showed an earlier tertiary phase and thus a shorter service life. The ratcheting strains also increase with increasing maximum stress, especially under torsion, and the influence of the mean stress is significant (Lu et al., 2016; Xi et al., 2015).

All the load cases are also compared under the same conditions: the maximum stress level at 50% of the strengths, stress ratio of $R = 0.1$, and service life at 90% of the service lives (before the tertiary stage). Although the different load frequencies of $f = 5, f = 1$, and $f = 0.05$ Hz are used under tension, torsion, and the multiaxial loads (squared, butterfly, and rhombic), respectively, the effect of the frequencies lower than 5 Hz on the ratcheting strains has been found to be small (Barriere et al., 2020). The results (ratcheting strains) are summarized in Fig. 12(e). It turns out that the differences between the observed and predicted results are small, and that torsional ratcheting is emphasized (cases 9–16). Thus, the amorphous polymer structure does not tolerate ratcheting in torsion as well as it does in tension. Despite this characteristic, the amorphous structure appears to resist fatigue damage under torsion well and produces considerable long service lives. The measured and predicted service lives are summarized in Fig. 12(f). Excluding case 10 for the highest tension, the service lives are accurately captured: the safety factor (factor that produces a lower life than observed) is less than 1.4 in all cases.

5. Summary

The short- to long-term uniaxial, torsional, and multiaxial deformation behaviors of amorphous polymers were tested and simulated. The effects of the mean stress, stress amplitude, loading rate, loading history, and loading mode on a common PC polymer were investigated. An improved testing equipment for injection was developed, and the tests were simulated by using an improved viscoelastic-viscoplastic constitutive model related to plastic flow and the free volume to accurately capture the nonlinear shear and multiaxial ratcheting behavior. Also, an improved fatigue damage model was proposed to predict fatigue lives under different loadings more accurately. With the fitted parameters, the proposed approach predicted all the test results well, suggesting that the approach is a capable tool for simulating costly tests.

It was observed, based on both the tests and model results, that (i) the amorphous polymer structure efficiently resists static creep and recovery under torsion. However (ii), the amorphous structure shows more ratcheting in torsion than in tension. Despite this characteristic, the amorphous structure appears to resist failure under cyclic torsion well. It was further observed that (iii) the ratcheting strains do not increase significantly until 90% of the service life is reached. Therefore, ratcheting behavior is an important precursory indicator for the drastic failure of engineering components that may cause horrific accidents and immense financial losses. Furthermore, (iv) the free volume (loosely packed regions of chains) strongly controls the development of plastic deformation and large ratcheting strains. Since crazing with the localized plastic deformation in the material develops owing to the nucleation of voids and an increased void volume fraction in regions with a high free volume (Venkatesan and Basu, 2015), crazing can be considered a precursor to plasticity and is essentially driven by the free volume. Finally, it was observed that (v) the development of the free volume and fatigue damage (fracturing of fibrils (Ravi Chandran, 2016)) strongly influence the tertiary cyclic creep at the end of the service life. The combined development of the free volume and fatigue damage was found to be similar to the development of void volume. Therefore, the service life of PC could be increased by restraining the development of void volume for example by optimizing the molding (pressure, temperature, and the size of the runner and gate of the mold) and using suitable additives (impact modifiers).

An important goal of future research will be to investigate microstructural changes (e.g., by employing X-ray tomography, positron annihilation methods or molecular dynamics simulations Poulsen et al., 2005; Venkatesan and Basu, 2015) vs. the development of the free volume that might correlate with our findings (iv) and (v). The results of this current work can be used to observe failure in practical structures, thereby allowing serious accidents to be predicted, and to develop more damage-tolerant and self-healing polymers (Patrick et al., 2016) for cyclic loads.

Data availability

The source data that support the findings of this study are available at https://doi.org/10.1016/j.ijplas.2021.103106. We provide the source data underlying Figs. 5b, c, f, and 8 c.

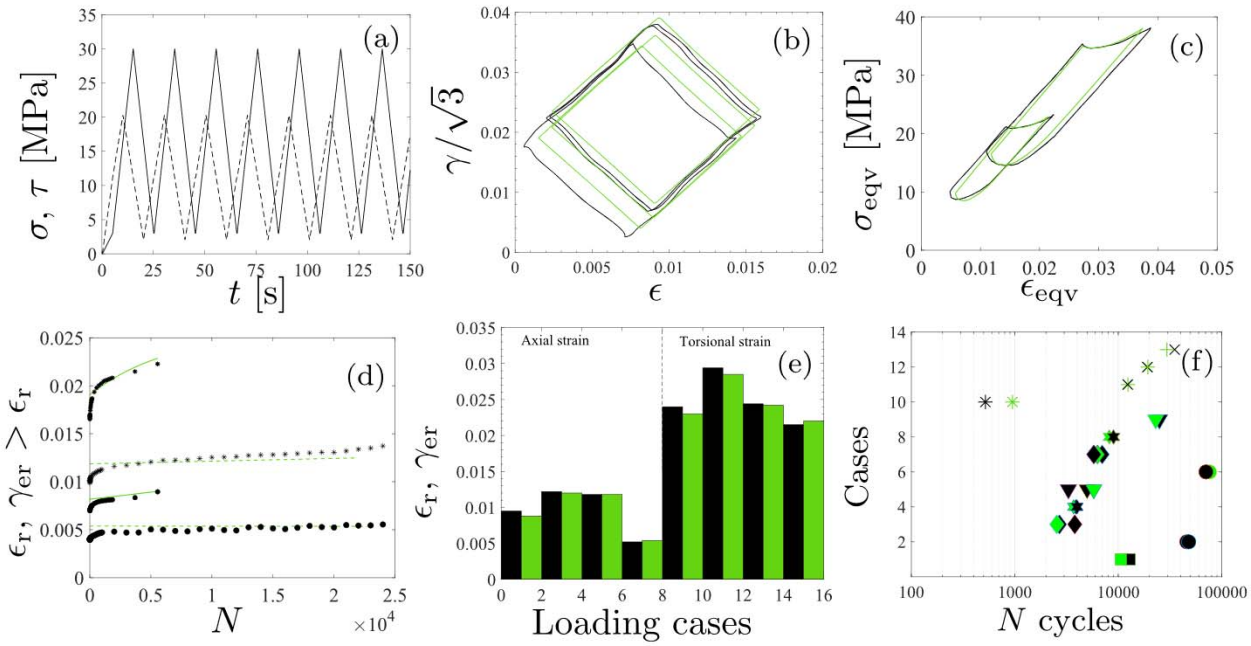

Fig. 12. Rhombic load path (a). Predicted (green) and measured (black) responses (b). The 100th, 1000th, and 5000th cycles are demonstrated. Measured (black) and predicted (green) 3000th loop of the equivalent strain vs. stress (c). Measured and predicted axial and shear ratcheting strains (rhombic) (d). Predicted (green) and measured (black) axial (cases 1–8) and torsional (cases 9–16) ratcheting strains under equivalent conditions (e). The loading cases 1 and 9 are tension and torsion, and cases 2–8 and 10–16 correspond to the squared, butterfly-type, and rhombic load paths, respectively. Measured (black) and predicted (green) service lives (f). Loading cases 1–5 correspond to the tensional, torsional, butterfly-type, squared, and rhombic load paths when the maximum stress level is 50%. Cases 6 to 9 are the same as 2 to 5, but the maximum stress is 30%. Case 10 is the tensional path when the maximum stress level is 97%. Cases 11–13 are the torsional load paths when the maximum stress levels are 82.5%, 75, and 65%. (For interpretation of the references to color in this figure legend, the reader is referred to the web version of this article.)

CRediT authorship contribution statement

T. Barriere: Conceptualization, Methodology, Funding acquisition, Validation, Formal analysis, Data curation, Writing – original draft, Writing – review & editing. **A. Cherouat:** Conceptualization, Methodology, Funding acquisition, Validation, Formal analysis, Data curation, Writing – original draft, Writing – review & editing. **X. Gabrion:** Conceptualization, Methodology, Funding acquisition, Validation, Formal analysis, Data curation, Writing – original draft, Writing – review & editing. **S. Holopainen:** Conceptualization, Methodology, Software, Validation, Formal analysis, Investigation, Data curation, Writing – original draft, Writing – review & editing, Visualization.

Declaration of Competing Interest

The authors declare that they have no known competing financial interests or personal relationships that could have appeared to influence the work reported in this paper.

Acknowledgments

The research was supported by the EIPHI Graduate School (contract ANR-17-EURE-0002) including its experimental facilities (manufacture of the thermoplastic mold and test specimens, Werth video-check, X-ray tomography, and optical 3D metrology). The authors acknowledge the technician Ly Phanousith from FEMTO-ST institute for conducting the experiments. The authors are grateful to MIFHySTO technological platform for the use of equipments. We want to show also thanks to Professors M. Ristinmaa (Lund Univ.), N-S Ottosen (Lund Univ.), and R. Kouhia (Tampere Univ.) for the fruitful discussions concerning fatigue modeling.

References

Abaqus, 2014. Abaqus Analysis User's Manual, Version 6.14. Technical report. Dassault Systémes Simulia Corp., Providence, RI, USA.
Adams, W.W., Farmer, B.L., Haines, J.P., 1998. A perspective on united states government-funded polymer research and development. Mater. Today 1, 25–30.
Anand, L., Ames, N.M., 2006. On modeling the micro-indentation response of an amorphous polymer. Int. J. Plast. 22, 1123–1170.
ASTM D638, 2003. Designation: D 638 - 03. Standard Test Method for Tensile Properties of Plastics. ASTM International, pp. 1–15.
ASTM E2207, 2002. Standard Practice for Strain-Controlled Axial-Torsional Fatigue Testing with Thin- Walled Tubular Specimens. ASTM International, pp. 1–8.

Bao, Q., Yang, Z., Lu, Z., 2020. Molecular dynamics simulation of amorphous polyethylene (PE) under cyclic tensile-compressive loading below the glass transition temperature. Polymer 186, 121968.
Barriere, T., Gabrion, X., Holopainen, S., 2019. A compact constitutive model to describe the viscoelastic-plastic behaviour of glassy polymers: comparison with monotonic and cyclic experiments and state-of-the-art models. Int. J. Plast. 122, 31–48.
Barriere, T., Gabrion, X., Holopainen, S., Jokinen, J., 2020. Testing and analysis of solid polymers under large monotonic and long-term cyclic deformation. Int. J. Plast. 135, 102781.
Bennett, T.D., Horike, S., 2018. Liquid, glass and amorphous solid states of coordination polymers and metal-organic frameworks. Nat. Rev. Mater. 3, 431–440.
Bowman, A.L., Mun, S., Nouranian, S., Huddleston, B., Gwaltney, S., Baskes, M., Horstemeyer, M., 2019. Free volume and internal structural evolution during creep in model amorphous polyethylene by molecular dynamics simulations. Polymer 170, 85–100.
Boyce, M.C., Arruda, E.M., Jayachandran, R., 1995. The large strain compression, tension, and simple shear of polycarbonate. Polym. Eng. Sci. 34, 716–725.
Boyce, M.C., Parks, D.M., Argon, A.S., 1988. Large inelastic deformation of glassy polymers, part I: rate-dependent constitutive model. Mech. Mater. 7, 15–33.
Buschow, K.H.J., et al., 2001. Encyclopedia of Materials: Science and Technology, first ed. Elsevier Ltd., pp. 7330–7341
Chaboche, J.L., Lesne, P.M., 1988. A non-linear continuous fatigue damage model. Fatigue Fract. Eng. Mater. Struct. 11, 1–17.
Chen, G., Liang, H.Q., Wang, L., Mei, Y.H., Chen, X., 2015. Multiaxial ratcheting-fatigue interaction on acrylonitrile-butadiene-styrene terpolymer. Polym. Eng. Sci. 55, 664–671.
Cherouat, A., Borouchaki, H., Jie, Z., 2018. Simulation of sheet metal forming processes using a fully rheological-damage constitutive model coupling and a specific 3D remeshing method. Metals 8, 1–38.
Colac, O.U., Dusunceli, N., 2006. Modeling viscoelastic and viscoplastic behavior of high density polyethylene (HDPE). ASME J. Eng. Mater. Technol. 128, 572–578.
Cubuk, E.D., Ivancic, R.J.S., Schoenholz, S.S., Strickland, D.J., 2017. Structure-property relationships from universal signatures of plasticity in disordered solids. Science 358, 1033–1037.
Dreistadt, C., Bonnet, A.S., Chevrier, P., Lipinski, P., 2009. Experimental study of the polycarbonate behaviour during complex loadings and comparison with the Boyce, Parks and Argon model predictions. Mater. Des. 30, 3126–3140.
Engqvist, J., Wallin, M., Ristinmaa, M., Hall, S.A., Plivelic, T.S., 2016. Modelling multi-scale deformation of amorphous glassy polymers with experimentally motivated evolution of the microstructure. J. Mech. Phys. Solids 96, 497–510.
Francis, D.K., Bouvard, J.L., Hammi, Y., Horstemeyer, M.F., 2014. Formulation of a damage internal state variable model for amorphous glassy polymers. Int. J. Solids Struct. 51, 2765–2776.
Frankberg, E.J., Kalikka, J., Ferrá, F.G., Joly-Pottuz, L., Salminen, T., Hintikka, J., Hokka, M., Koneti, S., Douillard, T., Saint, B.L., Kreiml, P., Cordill, M.J., Epicier, T., and, M.V.D.S., Roiban, L., Akola, J., Fonzo, F.D., Levänen, E., Masenelli-Varlot, K., 2019. Highly ductile amorphous oxide at room temperature and high strain rate. Science 366, 864–869.
Frondelius, T., Holopainen, S., Kouhia, R., Ottosen, N., Ristinmaa, M., Vaara, J., 2019. A continuum based macroscopic unified low-and high cycle fatigue model. MATEC Web Conf. 300, 16008.
Garcia-Gonzalez, D., Zaera, R., Arias, A., 2017. A hyperelastic-thermoviscoplastic constitutive model for semi-crystalline polymers: application to PEEK under dynamic loading conditions. Int. J. Plast. 88, 27–52.
Haouala, S., Doghri, I., 2015. Modeling and algorithms for two-scale time homogenization of viscoelastic-viscoplastic solids under large numbers of cycles. Int. J. Plast. 70, 98–125.
Haward, R.N., Thackray, G., 1968. The use of a mathematical model to describe isothermal stress-strain curves in glassy thermoplastics. Proc. R. Soc. A. 302, 453–472.
Holopainen, S., 2013. Modeling of the mechanical behavior of amorphous glassy polymers under variable loadings and comparison with state-of-the-art model predictions. Mech. Mater. 66, 35–58.
Holopainen, S., 2014. Influence of damage on inhomogeneous deformation behavior of amorphous glassy polymers. Modeling and algorithmic implementation in a finite element setting. Eng. Fract. Mech. 117, 28–50.
Holopainen, S., Barriere, T., 2018. Modeling of mechanical behavior of amorphous solids undergoing fatigue loadings, with application to polymers. Comput. Struct. 199, 57–73.
Holopainen, S., Barriere, T., Cheng, G., Kouhia, R., 2017. Continuum approach for modeling fatigue in amorphous glassy polymers. applications to the investigation of damage-ratcheting interaction in polycarbonate. Int. J. Plast. 91, 109–133.
Holopainen, S., Wallin, M., 2012. Modeling of long-term behavior of amorphous glassy polymers. ASME J. Eng. Mater. Technol. 135, 1–11.
Hughes, J.M., Lugo, M., Bouvard, J.L., McIntyre, T., Horstemeyer, M.F., 2017. Cyclic behavior and modeling of small fatigue cracks of a polycarbonate polymer. Int. J. Fatigue 99, 78–86.
James, M.N., Lu, Y., Christopher, C.J., Patterson, E.A., 2013. Crack path support for deformation mechanisms in fatigue of polycarbonate. Eng. Fract. Mech. 108, 89–97.
Janssen, R.P.M., Kanter, D.K., Govaert, L.E., Meijer, H.E.H., 2008. Fatigue life predictions for glassy polymers: aconstitutive approach. Macromolecules 41, 2520–2530.
Jiang, C., Zhu, Z., Zhang, J., Yang, Z., Jiang, H., 2020. Constitutive modeling of the rate- and temperature-dependent macro-yield behavior of amorphous glassy polymers. Int. J. Mech. Sci. 179, 105653.
Jiang, C.K., Jiang, H., Zhang, J.W., Kang, G.Z., 2015. A viscoelasticplastic constitutive model for uniaxial ratcheting behaviors of polycarbonate. Polym. Eng. Sci. 55, 2559–2565.
Jung, I.D., Shin, D.S., Kim, D., Lee, J., Lee, M.S., Son, H.J., Reddy, N.S., Kim, M., Moon, S., Kim, K.T., Yu, J.-H., Kim, S., Park, S.J., Sung, H., 2020. Artificial intelligence for the prediction of tensile properties by using microstructural parameters in high strength steels. Materialia 11, 100699.
Kang, G., Kan, Q., 2017. Cyclic Plasticity of Engineering Materials: Experiments and Models. John Wiley & Sons, Chichester.
Kanters, M.J.W., Kurokawa, T., Govaert, L.E., 2016. Competition between plasticity-controlled and crack-growth controlled failure in static and cyclic fatigue of thermoplastic polymer systems. Polym. Test. 50, 101–110.
Krairi, A., Doghri, I., 2014. A thermodynamically-based constitutive model for thermoplastic polymers coupling viscoelasticity, viscoplasticity and ductile damage. Int. J. Plast. 60, 163–181.
Krairi, A., Doghri, I., Schalnat, J., Robert, G., Paepegem, W.V., 2019. Thermo-mechanical coupling of a viscoelastic-viscoplastic model for thermoplastic polymers: thermodynamical derivation and experimental assessment. Int. J. Plast. 115, 154–177.
Lei, Z., Wu, P., 2019. A highly transparent and ultra-stretchable conductor with stable conductivity during large deformation. Nat. Commun. 10, 3429.
Lemaitre, J., Chaboche, J.L., 1999. Mechanics of Solid Materials. Cambridge University Press, Cambridge.
Lindström, S.B., Thore, C.-J., Suresh, S., Klarbring, A., 2020. Continuous-time, high-cycle fatigue model: validity range and computational acceleration for cyclic stress. Int. J. Fatigue 136, 105582.
Losi, G., Knauss, W.G., 1992. Free volume theory and nonlinear thermoviscoelasticity. Polym. Eng. Sci. 32, 542–557.
Lu, F., Kang, G., Zhu, Y., Xi, C., Jiang, H., 2016. Experimental observation on multiaxial ratchetting of polycarbonate polymer at room temperature. Polym. Test. 50, 135–144.
Lugo, M., Fountain, J.E., Hughes, J.M., Bouvard, J.-L., Horstemayer, M.F., 2014. Microstructure-based fatigue modeling of an acrylonitrile butadiene styrene (ABS) copolymer. J. Appl. Polym. 131, 1–12.
Ottosen, N., Stenström, R., Ristinmaa, M., 2008. Continuum approach to high-cycle fatigue modeling. Int. J. Fatigue 30, 996–1006.
Park, S.-A., Jeon, H., Kim, H., Shin, S.-H., Choy, S., Hwang, D.S., Koo, J.M., Jegal, J., Hwang, S.Y., Park, J., Oh, D.X., 2019. Sustainable and recyclable super engineering thermoplastic from biorenewable monomer. Nat. Commun. 10, 2601–2611.
Pastukhov, L.V., Kanters, M.J.W., Engels, T.A.P., Govaert, L.E., 2020. Physical background of the endurance in poly(ether ether ketone). J Polym Sci. 1–21.
Patrick, J.F., Robb, M.J., Sottos, N.R., Moore, J.S., White, S.R., 2016. Polymers with autonomous life-cycle control. Nature 540, 363–370.
Poulsen, H.F., Wert, J.A., Neuefeind, J., Honkimäki, V., Daymond, M., 2005. Measuring strain distributions in amorphous materials. Nat. Mater. 4, 1–4.

Praud, F., Chatzigeorgiou, G., Bikard, J., Meraghni, F., 2017. Phenomenological multi-mechanisms constitutive modelling for thermoplastic polymers, implicit implementation and experimental validation. Mech. Mater. 114, 9–29.
Press, W.H., Teukolsky, S.A., 2007. Numerical Recipes 3rd Edition: The Art of Scientific Computing. Cambridge University Press, 40W. 20 St. New York, NY, United States.
Qi, Z., Hu, N., Li, G., Zeng, D., Su, X., 2019. Constitutive modeling for the elastic-viscoplastic behavior of high density polyethylene under cyclic loading. Int. J. Plast. 113, 125–144.
Ravi Chandran, K.S., 2016. Mechanical fatigue of polymers: a new approach to characterize the S-N behavior on the basis of macroscopic crack growth mechanism. Polymer 91, 222–238.
Sadd, M., 2018. Continuum Mechanics Modeling of Material Behavior, first ed. Academic Press.
Shojaei, A.K., Volgers, P., 2018. A coupled hyperelastic-plastic-continuum damage model for studying cyclic behavior of unfilled engineering polymers. Int. J. Fatigue 107, 33–39.
Sun, Y., Concustell, A., Gree, A.L., 2016. Thermomechanical processing of metallic glasses: extending the range of the glassy state. Nat. Rev. Mater. 1, 1–14.
Venkatesan, S., Basu, S., 2015. Investigations into crazing in glassy amorphous polymers through molecular dynamics simulations. J. Mech. Phys. Solids 77, 123–145.
Vernerey, F.J., Brighenti, R., Long, R., Shen, T., 2018. Statistical damage mechanics of polymer networks. Macromolecules 51, 6609–6622.
Wang, J., Peng, L., Deng, Y., Lai, X., Fu, M., Ni, J., 2019. A finite strain thermodynamically-based constitutive modeling and analysis of viscoelastic-viscoplastic deformation behavior of glassy polymers. Int. J. Plast. 122, 135–163.
Wang, J., Xu, Y., Zhang, W., Moumni, Z., 2016. A damage-based elastic-viscoplastic constitutive model for amorphous glassy polycarbonate polymers. Mater. Des. 97, 519–531.
Wu, P.D., Giessen, E.V.d., 1993. On improved network models for rubber elasticity and their applications to orientation hardening in glassy polymers. J. Mech. Phys. Solids 41, 427–456.
Xi, C., Kang, G., Lu, F., Zhang, J., Jiang, H., 2015. An experimental study on uniaxial ratcheting of polycarbonate polymers with different molecular weights. Mater. Des. 67, 644–648.